Geochemistry, Geophysics, Geosystems®

AGU ADVANCING EARTH AND SPACE SCIENCE

RESEARCH ARTICLE
10.1029/2021GC010133

Key Points:

- Four down-core diagenetic zones are identified with magnetic mineral assemblages reflecting sediment provenance and diagenetic processes
- Limited exposure of sediments to dissolved sulfide due to rapid burial leads to greigite preservation in the upper ~460 m
- High-temperature diagenetic processes are responsible for later iron oxide formation and reduction in deeper sediments

Supporting Information:

Supporting Information may be found in the online version of this article.

Correspondence to:

M. Kars,
mkars@kochi-u.ac.jp

Citation:

Kars, M., Köster, M., Henkel, S., Stein, R., Schubotz, F., Zhao, X., et al. (2021). Influence of early low-temperature and later high-temperature diagenesis on magnetic mineral assemblages in marine sediments from the Nankai Trough. *Geochemistry, Geophysics, Geosystems*, *22*, e2021GC010133. https://doi.org/10.1029/2021GC010133

Received 30 AUG 2021
Accepted 13 OCT 2021

Author Contributions:

Conceptualization: Myriam Kars, Male Köster
Funding acquisition: Myriam Kars
Methodology: Myriam Kars, Rüdiger Stein, Xiang Zhao, Stephen A. Bowden
Supervision: Myriam Kars
Validation: Stephen A. Bowden
Writing – original draft: Myriam Kars, Male Köster, Susann Henkel, Rüdiger Stein, Stephen A. Bowden
Writing – review & editing: Myriam Kars, Male Köster, Susann Henkel, Rüdiger Stein, Stephen A. Bowden, Andrew P. Roberts, Kazuto Kodama

Influence of Early Low-Temperature and Later High-Temperature Diagenesis on Magnetic Mineral Assemblages in Marine Sediments From the Nankai Trough

Myriam Kars[1], Male Köster[2], Susann Henkel[2,3], Rüdiger Stein[2,3], Florence Schubotz[3], Xiang Zhao[4], Stephen A. Bowden[5], Andrew P. Roberts[4], and Kazuto Kodama[6]

[1]Center for Advanced Marine Core Research, Kochi University, Nankoku, Japan, [2]Alfred Wegener Institute, Helmholtz Centre for Polar and Marine Research, Bremerhaven, Germany, [3]MARUM—Center for Marine Environmental Sciences, University of Bremen, Bremen, Germany, [4]Research School of Earth Sciences, Australian National University, Canberra, ACT, Australia, [5]School of Geosciences, University of Aberdeen, Aberdeen, UK, [6]Research Center for Knowledge Science in Cultural Heritage, Doshisha University, Kyoto, Japan

Abstract Diagenesis can have a major impact on sedimentary mineralogy. Primary magnetic mineral assemblages can be modified significantly by dissolution or by formation of new magnetic minerals during early or late diagenesis. At International Ocean Discovery Program Site C0023, which was drilled in the protothrust zone of the Nankai Trough during Expedition 370, offshore of Shikoku Island, Japan, non-steady state conditions have produced a complex sequence of magnetic overprints. Detailed rock magnetic measurements, which characterize magnetic mineral assemblages in terms of abundance, grain size, and composition, were conducted to assess magnetic mineral alteration and diagenetic overprinting. Four magnetic zones (MZs) are identified down-core from ~200 to 1,100 m below sea floor based on rock magnetic variations. MZ 1 is a high magnetic intensity zone that contains ferrimagnetic greigite, which formed at shallow depths and is preserved because of rapid sedimentation. MZs 2 and 4 are low magnetic intensity zones with fewer magnetic minerals, mainly coarse-grained (titano-)magnetite and hematite. This magnetic mineral assemblage is a remnant of a more complex assemblage that was altered diagenetically a few million years after deposition when the site entered the Nankai Trough. MZ 3 is a high magnetic intensity zone between MZs 2 and 4. It contains authigenic single-domain magnetic particles that probably formed from fluids that circulated through faults in the accretionary prism. Varying sediment supply and organic matter input through time, burial temperature, and tectonic fluid circulation are the primary drivers of magnetic mineral assemblage variations.

1. Introduction

Dissimilatory iron reduction plays an important role in iron cycling in reducing environments (e.g., Lovley, 1991). Detrital and authigenic iron oxides are used by microbes as electron acceptors to oxidize organic matter, releasing dissolved iron (Fe^{2+}) into porewater. In marine environments, early formation of authigenic iron oxides results from Fe^{2+} diffusion into the overlying oxic and nitrogenous zones. In underlying sulfidic environments, dissolved iron and iron-bearing solid phases react with dissolved sulfide (HS^-/H_2S) to form iron sulfides. HS^-/H_2S results from organoclastic sulfate reduction associated with organic matter decomposition (e.g., R. A. Berner, 1981; Jørgensen et al., 2019) and microbial anaerobic oxidation of methane (AOM) above and at the sulfate-methane transition (SMT) zone (e.g., Knittel & Boetius, 2009; Treude et al., 2005). These processes strongly affect iron-bearing magnetic minerals, which affects the magnetic properties of sediments and sedimentary rocks (Roberts, 2015). Iron reduction and the subsequent incorporation of released Fe^{2+} into iron sulfides, is an important mechanism responsible for magnetic mineral alteration. Destruction of detrital and biogenic ferrimagnetic minerals during diagenesis can destroy primary magnetic records. Limited exposure of sediments to dissolved sulfide can prevent pyritization (e.g., R. A. Berner, 1984; Canfield & Berner, 1987) and favor preservation of metastable iron sulfide precursors such as greigite (Kao et al., 2004). Greigite is ferrimagnetic and can carry a secondary magnetization that can poten-

tially obscure the original paleomagnetic record (Roberts & Weaver, 2005; Rowan & Roberts, 2005; Rowan et al., 2009). Generally, the presence of greigite indicates environments with limited availability of dissolved sulfide, such as in gas hydrate-bearing zones (e.g., Housen & Musgrave, 1996; Larrasoaña et al., 2007; Kars & Kodama, 2015a, 2015b), which lie below the sulfidic zone (Roberts, 2015).

The Nankai Trough and its accretionary complex are located southwest of Japan (Figure 1a) and have been intensively studied to understand earthquake mechanisms and tsunami generation (NanTroSEIZE project). It is also ideal for studying the deep biosphere and the temperature limit of life due to exceptionally high prevailing heat flow. After Ocean Drilling Program (ODP) Leg 131 (Taira et al., 1991) and ODP Leg 190 (Moore et al., 2001), International Ocean Discovery Program (IODP) Expedition 370 drilled Site C0023 offshore of Cape Muroto, Shikoku Island, Japan (Heuer, Inagaki, Morono, Kubo, Maeda, & the Expedition 370 Scientists, 2017). This expedition mainly aimed to investigate the temperature limit of life in marine sediments. Site C0023 (Hole C0023A) is a 1.2-km borehole that was drilled using D/V *Chikyu* close to Site 1174 of ODP Leg 190 (Figure 1b). Parkes et al. (2007) showed that methanogen activity at Site 1174 is enhanced by adding iron oxides (magnetite and ferrihydrite) into the medium, which led to increased methane release. The process by which iron and methane are coupled is not fully understood. Aromokeye et al. (2021) suggested that during methanogenic benzoate degradation, crystalline Fe oxides serve as conduits for microbes and are reduced to contributing to the Fe^{2+} pool in methanogenic marine sediments. Reduction of Fe^{3+}-bearing magnetic minerals by microbial activity affects magnetic mineral assemblages to extents that remain unassessed (e.g., Riedinger et al., 2005, 2010). Here, we present a detailed rock magnetic study of diagenetic events at Site C0023. The sensitivity of magnetic minerals to biogeochemical processes makes them useful for investigating magnetic mineral assemblage variations to obtain new insights into environmental conditions. Microbial activity, high burial temperature, and fluid circulation through faults are the main investigated processes to understand magnetic mineralogy variations at Site C0023.

2. Materials and Methods

2.1. Geologic Setting and Materials

The Nankai Trough formed by subduction of the Philippine Sea Plate beneath the Eurasian Plate. The Nankai Accretionary Complex formed by scraping of sediment from the descending plate, which has a current subduction rate of ~2–4 cm/yr (Seno et al., 1993; Figure 1a). Three major scientific ocean drilling transects have been sampled: the Ashizuri and Muroto transects offshore of Shikoku Island (e.g., Moore et al., 2001; Taira et al., 1991) and the Kumano transect (NanTroSEIZE) off Kii peninsula (e.g., Kinoshita et al., 2009). IODP Expedition 370 drilled Site C0023 (32°22.00'N, 134°57.98'E, water depth: 4,776 m) in the protothrust zone of the prism, near ODP Leg 131 Site 808 and ODP Leg 190 Site 1174 in the Muroto transect (Figure 1b). Site C0023 is at the seaward end of the Nankai accretionary prism. At this site, ~16 Ma basaltic basement is overlain from bottom to top by a volcaniclastic facies (Lithologic Unit V, 1,125.9–1,112 meters below seafloor [mbsf]), the Lower Shikoku Basin facies (hemipelagic mudstone, Unit IV, 1,112–637.25 mbsf) that includes the décollement zone of the accretionary prism with reverse faults that pass through the core (~758–796 mbsf), the Upper Shikoku Basin facies (hemipelagic bioturbated mudstones with numerous ash layers, Unit III, 637.25–494 mbsf), a trench-to-basin transitional facies (Subunit IIC, 494–428 mbsf), an outer trench-wedge facies (Subunit IIB, 428–353 mbsf), and an axial trench-wedge facies (Subunit IIA, 318.5–189 mbsf) that consists mainly of sand and turbidites, with hemipelagic mud and volcaniclastic sediment (Subunit IIC) (Figures 2 and S1 in Supporting Information S1; Heuer, Inagaki, Morono, Kubo, Maeda, Bowden, et al., 2017). Shallower sediments (<189 mbsf) were not recovered during IODP Expedition 370. Paleomagnetic samples (225 samples) were taken from hemipelagic fine-grained mudstones in 7-cm^3 plastic boxes from cores 3F to 86R (~206–892 mbsf). In more lithified lithologies, 10-cm^3 mini-cores were drilled from cores 87R to 107R (~900–1,099 mbsf).

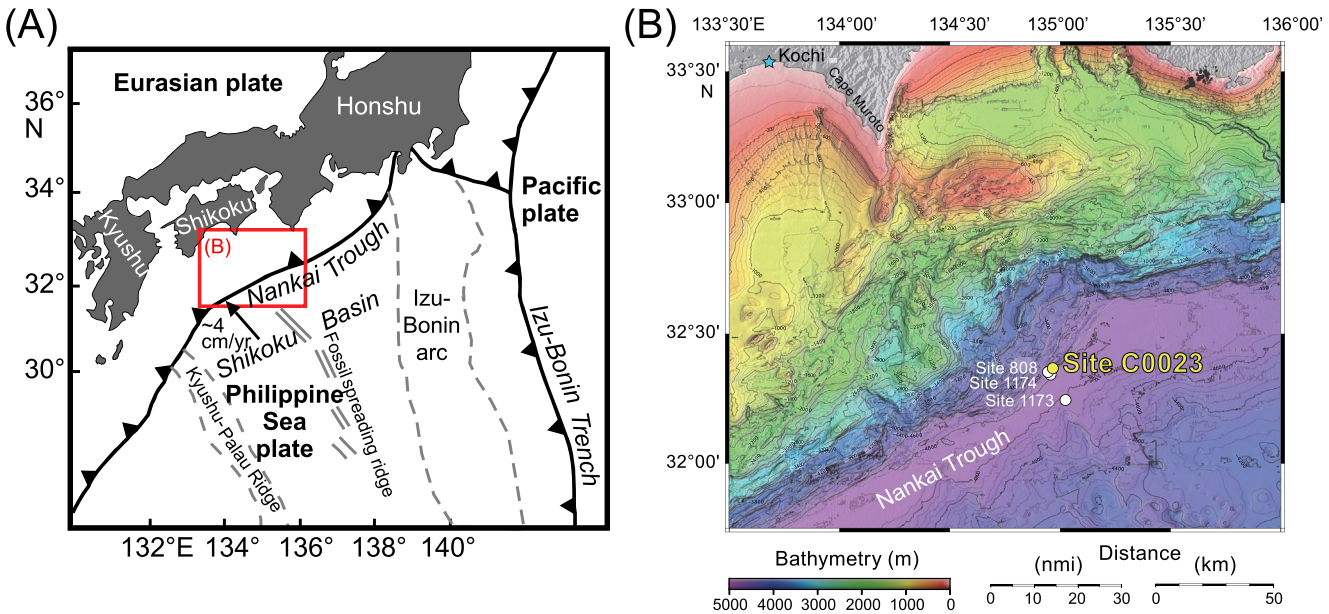

Figure 1. (a) General tectonic configuration of the Japanese islands. The red box is the area indicated in (b), which is a regional bathymetric map around Site C0023, International Ocean Discovery Program Expedition 370, with nearby Ocean Drilling Program Sites 808, 1174, and 1173 (modified after Heuer, Inagaki, Morono, Kubo, Maeda, & the Expedition 370 Scientists, 2017).

2.2. Methods

2.2.1. Rock Magnetic Measurements

All rock magnetic measurements were made at the Center for Advanced Marine Core Research (Kochi University, Japan) unless stated otherwise. Low-field, low-frequency (0.465 kHz) and low-field, high-frequency (4.65 kHz) magnetic susceptibility (χ_{lf} and χ_{hf}, respectively) measurements were made with a MS2B Bartington Instruments magnetic susceptibility meter (field = 250 μT). The frequency-dependent susceptibility χ_{fd} (%) (= $(\chi_{lf}-\chi_{hf})/\chi_{lf} \times 100$) is used as a proxy for small (superparamagnetic, SP) particles. The natural remanent magnetization (NRM) and an anhysteretic remanent magnetization (ARM) were measured with a 2-G Enterprises 760R cryogenic magnetometer in a shielded paleomagnetic laboratory. ARM was imparted in a direct current (DC) bias field of 50 μT in the presence of an 80 mT peak alternating field (AF). A saturation isothermal remanent magnetization (SIRM) was subsequently imparted to samples along the $+z$ direction at 1.2 T using a MMPM10 impulse magnetizer before being analyzed with a Natsuhara Giken spinner magnetometer. The samples were then remagnetized along the $-z$ direction with DC fields of 0.1 and 0.3 T and were measured again to calculate $S_{-0.1T}$ and $S_{-0.3T}$ (= $[(-IRM_{-0.3T})/SIRM) + 1]/2$; Bloemendal et al., 1992), which indicate the relative proportion of high coercivity minerals (e.g., hematite, goethite, some ferrimagnetic iron sulfides) in mixtures with soft ferrimagnetic minerals (e.g., magnetite, maghemite).

Hysteresis loops were measured to 1-T maximum applied fields on dry sediment powdered sister samples at room temperature with a Princeton Measurements Corporation (PMC) vibrating sample magnetometer (VSM). The saturation magnetization (M_s), saturation remanent magnetization (M_{rs}), and coercivity (B_c) were derived from the loops. Saturation was assumed above 70% of the maximum applied field, which might underestimate M_{rs}/M_s (Roberts et al., 2018 and references therein). The coercivity of remanence (B_{cr}) was determined from backfield demagnetization curves of M_{rs}. Conventional first-order reversal curves (FORCs; Pike et al., 1999) were measured for 91 samples selected at ~5–10-m stratigraphic intervals, with a 1-T saturating field (100 ms averaging time; 4 mT field increment; 91 FORCs). Regular FORC diagrams with evenly spaced field steps were processed using the FORCinel software (Harrison & Feinberg, 2008)

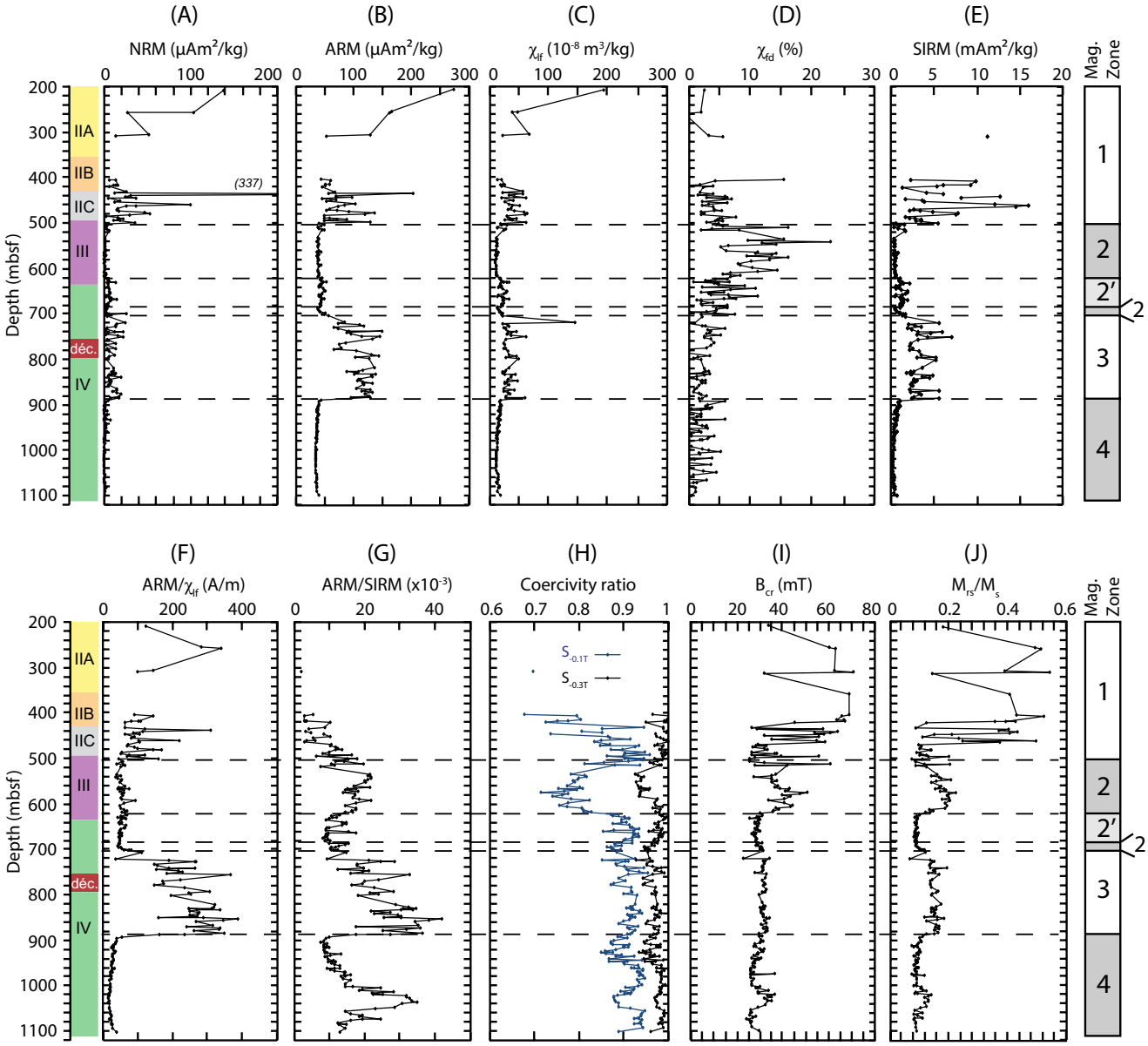

Figure 2. Down-core rock magnetic and coercivity variations at Site C0023. (a) Natural remanent magnetization (NRM), (b) anhysteretic remanent magnetization (ARM), (c) magnetic susceptibility χ_{lf}, (d) frequency-dependent susceptibility χ_{fd}, (e) saturation isothermal remanent magnetization (SIRM), (f) ARM/χ_{lf}, (g) ARM/SIRM, (h) coercivity ratios, (i) remanent coercivity B_{cr}, and (j) M_{rs}/M_s. Discrete sample measurements are shown in (a–h), whereas (i and j) are dry powder sister sample measurements. Four major magnetic zones (MZs), indicated on the right, are identified from magnetic changes. MZs 1 and 3 correspond to higher magnetic mineral concentrations; MZs 2 and 4 correspond to lower concentrations. On the left, the Lithologic Units (IIA to IV) and décollement ("déc.") are from Heuer, Inagaki, Morono, Kubo, Maeda, Bowden, et al. (2017).

with constant smoothing factor, SF. Twenty-one samples were selected for irregular FORCs measurements. Irregularly spaced field steps enable use of different resolutions for different parts of a FORC diagram (Zhao et al., 2015). Irregular FORCs were measured at the Australian National University with a PMC VSM. Remanent FORC (remFORC), transient FORC (tFORC), and induced FORC (iFORC) diagrams were processed following the approach of Zhao et al. (2017). FORC diagrams measured with regularly spaced field steps for samples shown in Figures 3–6 are in Supporting Information S1.

Low-temperature magnetic measurements (from 300 to 10 K) were made with a Quantum Design Magnetic Properties Measurement System (MPMS) for 18 selected samples. The samples each have ~100–120 mg

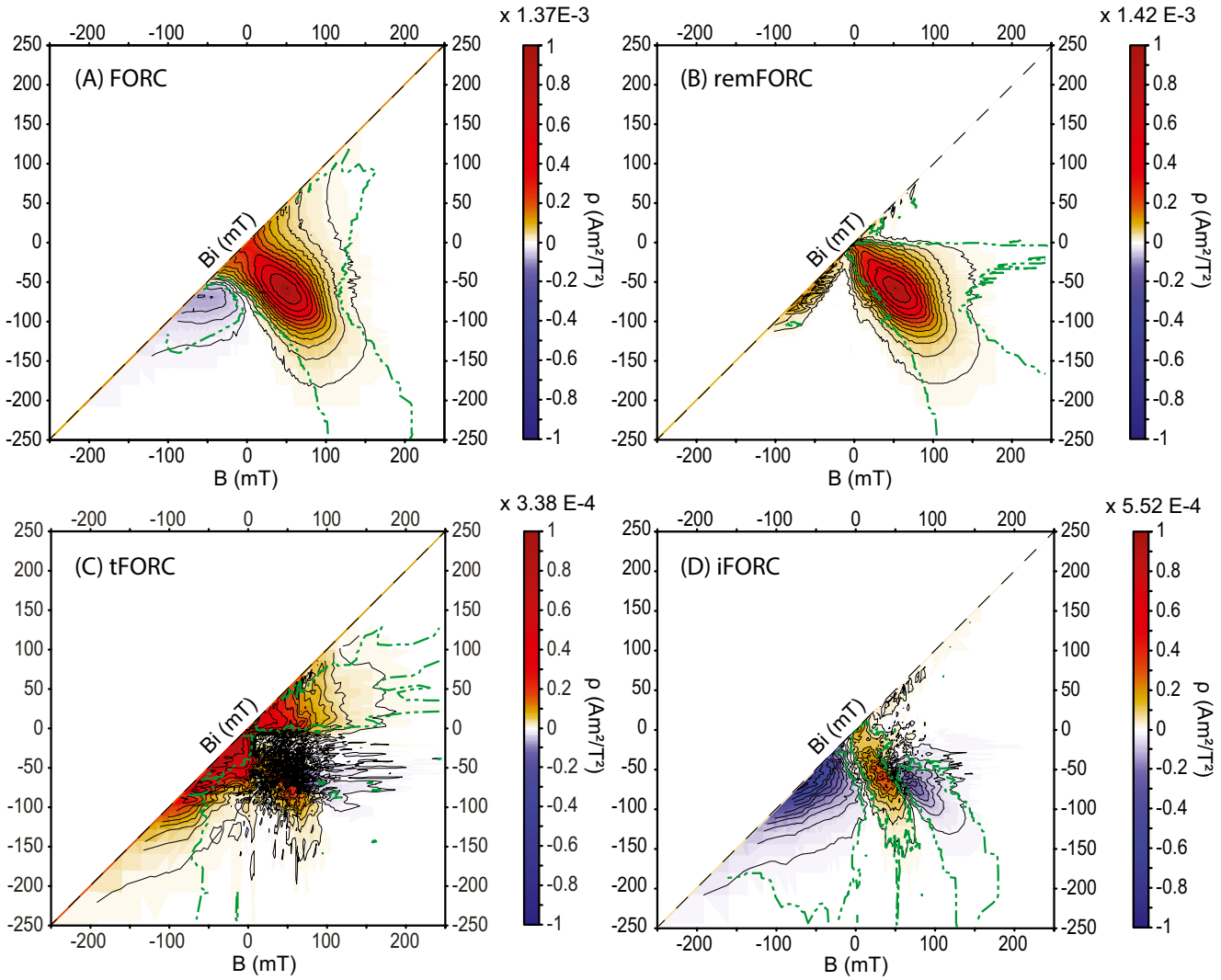

Figure 3. First-order reversal curve (FORC)-type diagrams for Sample 370-C0023A-7X-1W, 32–34 cm (depth: 305.32 meters below seafloor) in Magnetic Zone (MZ) 1. (a) Conventional FORC diagram, (b) remanent FORC (remFORC) diagram, (c) transient hysteresis FORC (tFORC) diagram, and (d) induced FORC (iFORC) diagram. This sample has high coercivity (B_{cr} = 62 mT). Green contours indicate the 0.05 significance level for the FORC distributions calculated according to Heslop and Roberts (2012). Complementary rock magnetic data discussed in the text for this sample are shown in Figure S3 in Supporting Information S1. See Figures S3 and S4 in Supporting Information S1 for a low coercivity (B_{cr} = 28 mT) sample from MZ 1.

mass and were dried, ground lightly to a fine powder, and sealed in a gelatin capsule before being measured. A room temperature SIRM (RT-SIRM) was acquired at 2.5 T. A 300-10-300 K cooling-warming cycle of the RT-SIRM was then carried out in zero magnetic field (<20 μT) trapped within the MPMS. A low-temperature SIRM (LT-SIRM) was imparted at 10 K at 2.5 T and samples were then warmed to room temperature in zero magnetic field and measured (termed ZFC for zero-field-cooled). Samples were subsequently cooled to 10 K in a 2.5 T magnetic field and the LT-SIRM was analyzed during warming to 300 K (termed FC for field-cooled). Thermomagnetic experiments in vacuum were made on 40 selected specimens with a Natsuhara Giken NMB-89 magnetic balance from room temperature to 700°C (at a heating rate of 10°C/min in a 0.3 T field).

2.2.2. Rock-Eval Pyrolysis

Rock-Eval pyrolysis allows determination of the quantity, type, and thermal maturity of organic matter (e.g., Espitalié et al., 1977; Peters, 1986; Stein et al., 1986; Tissot & Welte, 1984). Our measurements were made with a Rock-Eval 6 analyzer (cf. Behar et al., 2001) at the Alfred Wegener Institute, Germany (Stein, 2021).

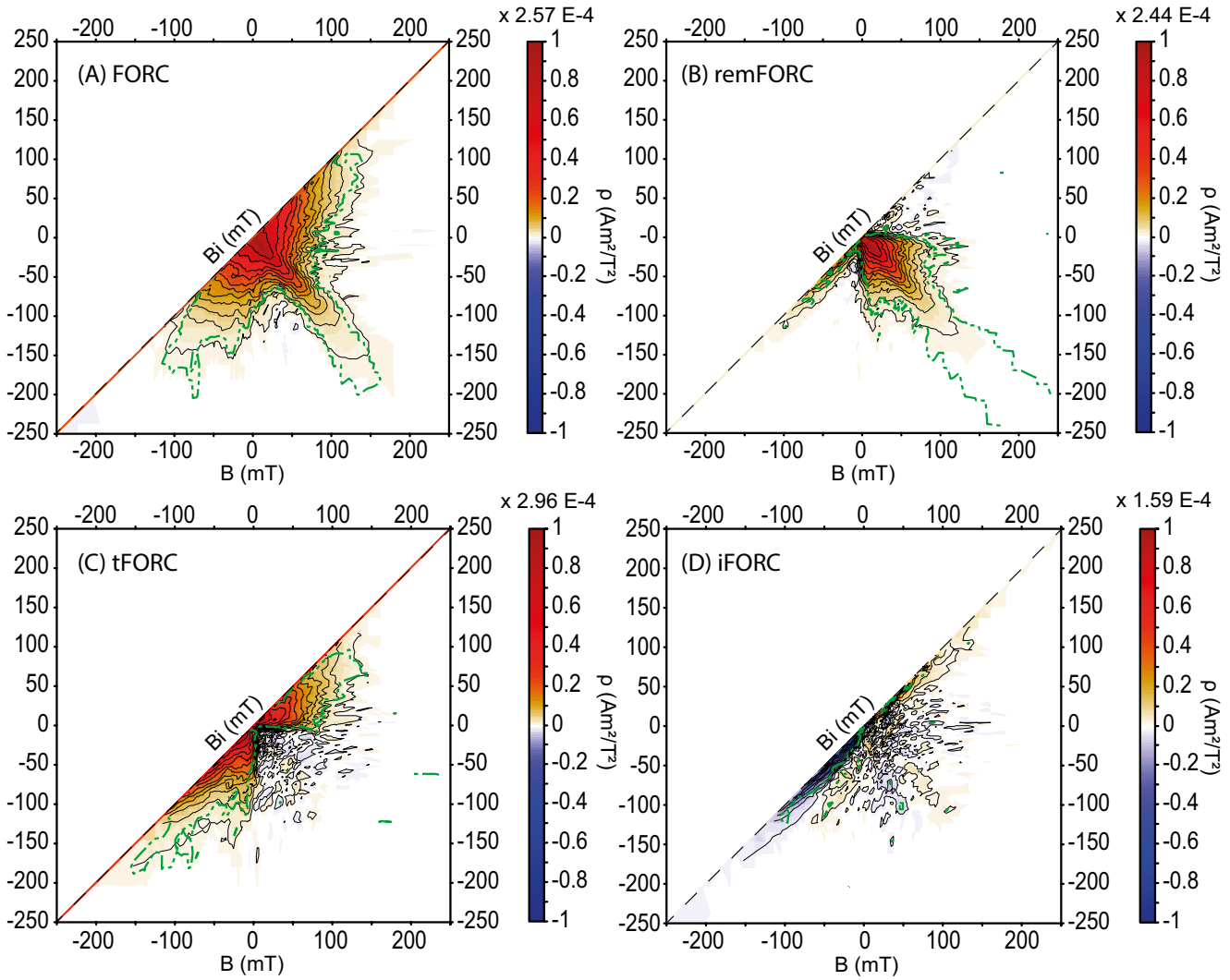

Figure 4. First-order reversal curve (FORC)-type diagrams for Sample 370-C0023A-50R-5W, 40–42 cm (depth: 696.53 meters below seafloor) in Magnetic Zone 2. (a) Conventional FORC diagram, (b) remanent FORC (remFORC) diagram, (c) transient hysteresis FORC (tFORC) diagram, and (d) induced FORC (iFORC) diagram. Green contours indicate the 0.05 significance level for the FORC distributions calculated according to Heslop and Roberts (2012). Complementary rock magnetic data discussed in the text for this sample are shown in Figure S5 in Supporting Information S1.

Pyrolysis was conducted on ground bulk sediment samples (100 mg/sample) to determine (a) the hydrocarbon (HC) content (S1 peak in mgHC/g of sediment), (b) the amount of HC generated by pyrolytic degradation of kerogen during heating to 550°C (S2 peak in mgHC/g of sediment), (c) the amount of carbon dioxide (CO_2) generated during heating to 390°C (S3 peak in mgCO_2/g of sediment), and (d) the temperature of maximum pyrolysis yield (T_{max} value in °C). T_{max} values <435°C are indicative of immature organic matter. Total organic carbon values of the analyzed sediments are known from shipboard measurements (Heuer, Inagaki, Morono, Kubo, Maeda, Bowden, et al., 2017).

2.2.3. Basin Modeling

Basin modeling at Site C0023 was performed with the Petromod 2017 package (Tsang et al., 2020). A 1D model was constructed using lithological and biostratigraphic information from Heuer, Inagaki, Morono, Kubo, Maeda, and the Expedition 370 Scientists (2017) and Hagino and the Expedition 370 Scientists (2018). Inbuilt libraries of formation properties were used to match thermal conductivity and porosity measurements, which yields a better match to physical aspects than previous modeling (Horsfield et al., 2006) and basin modeling studies in general (where thermal conductivity is not measured at high resolution or not

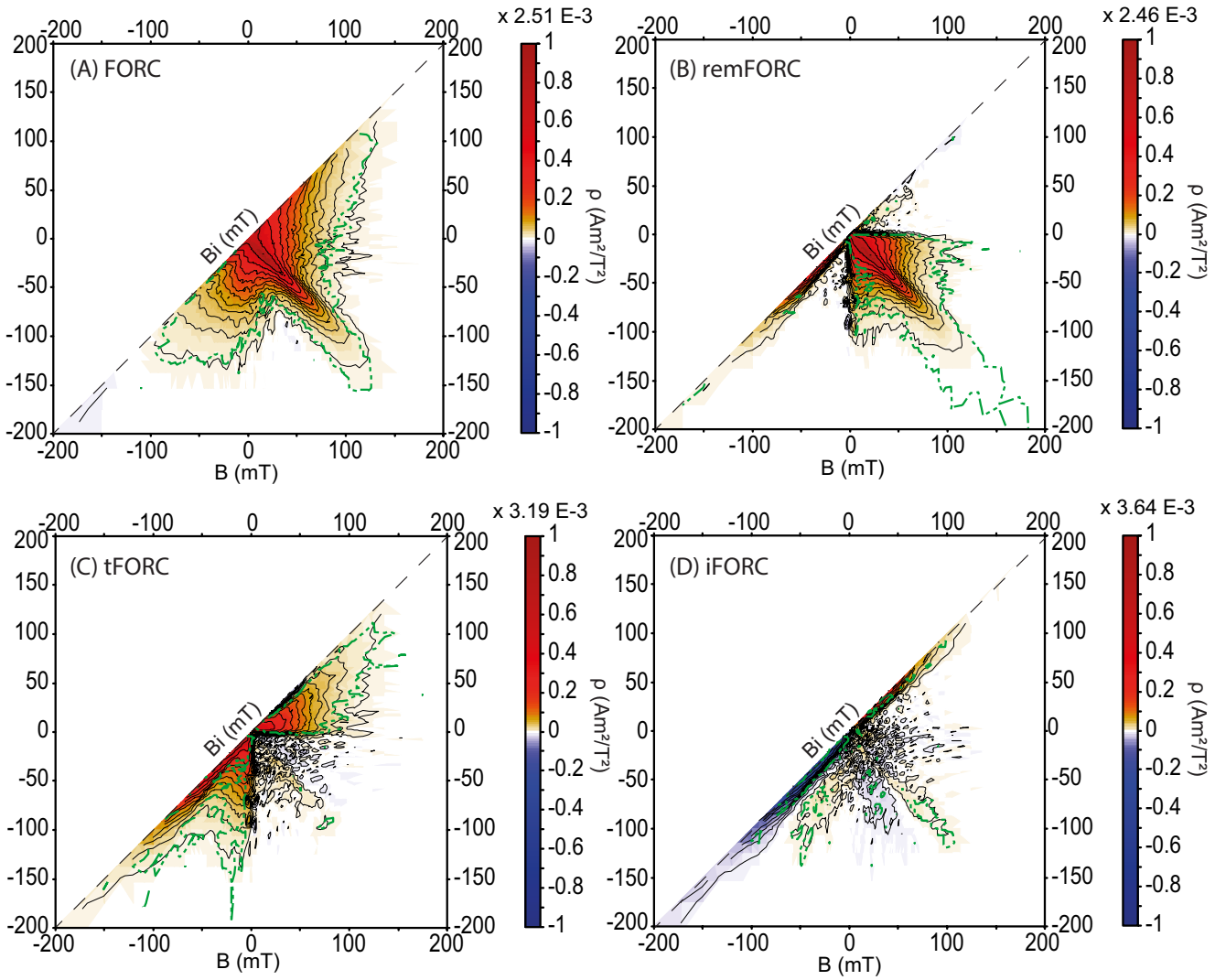

Figure 5. First-order reversal curve (FORC)-type diagrams for Sample 370-C0023A-61R-3W, 70–72 cm (depth: 750.51 meters below seafloor) in Magnetic Zone 3. (a) Conventional FORC diagram, (b) remanent FORC (remFORC) diagram, (c) transient hysteresis FORC (tFORC) diagram, and (d) induced FORC (iFORC) diagram. Green contours indicate the 0.05 significance level for the FORC distributions calculated according to Heslop and Roberts (2012). Complementary rock magnetic data discussed in the text for this sample are shown in Figure S6 in Supporting Information S1.

measured at all). The model was calibrated and conditioned to reproduce present-day temperatures and measured thermal maturities (biomarker parameters for pre-oil window thermal maturities and unpublished vitrinite reflectance). Present-day heat flow at Site C0023 is 140 mW/m^2 (shipboard results in Heuer, Inagaki, Morono, Kubo, Maeda, Bowden, et al., 2017). Model boundary conditions and other time-variant aspects are detailed by Tsang et al. (2020); in brief, paleo-seafloor temperature was fixed to the present-day value of 2°C (the site has been continuously in deep water since basement formation) and past heat flows are taken from analog environments and modern observations in the region (Tsang et al., 2020 and references therein).

3. Results

NRM, ARM, magnetic susceptibility χ_{lf}, and SIRM are widely used as magnetic mineral concentration proxies. In ODP Leg 131 (Shipboard Scientific Party, 1991) and Leg 190 sites (Shipboard Scientific Party, 2001), which were drilled next to Site C0023, these parameters were used to define sediment magnetic zones (MZs). Site C0023 has similar down-core variations with four main MZs (Figure 2, Table S1

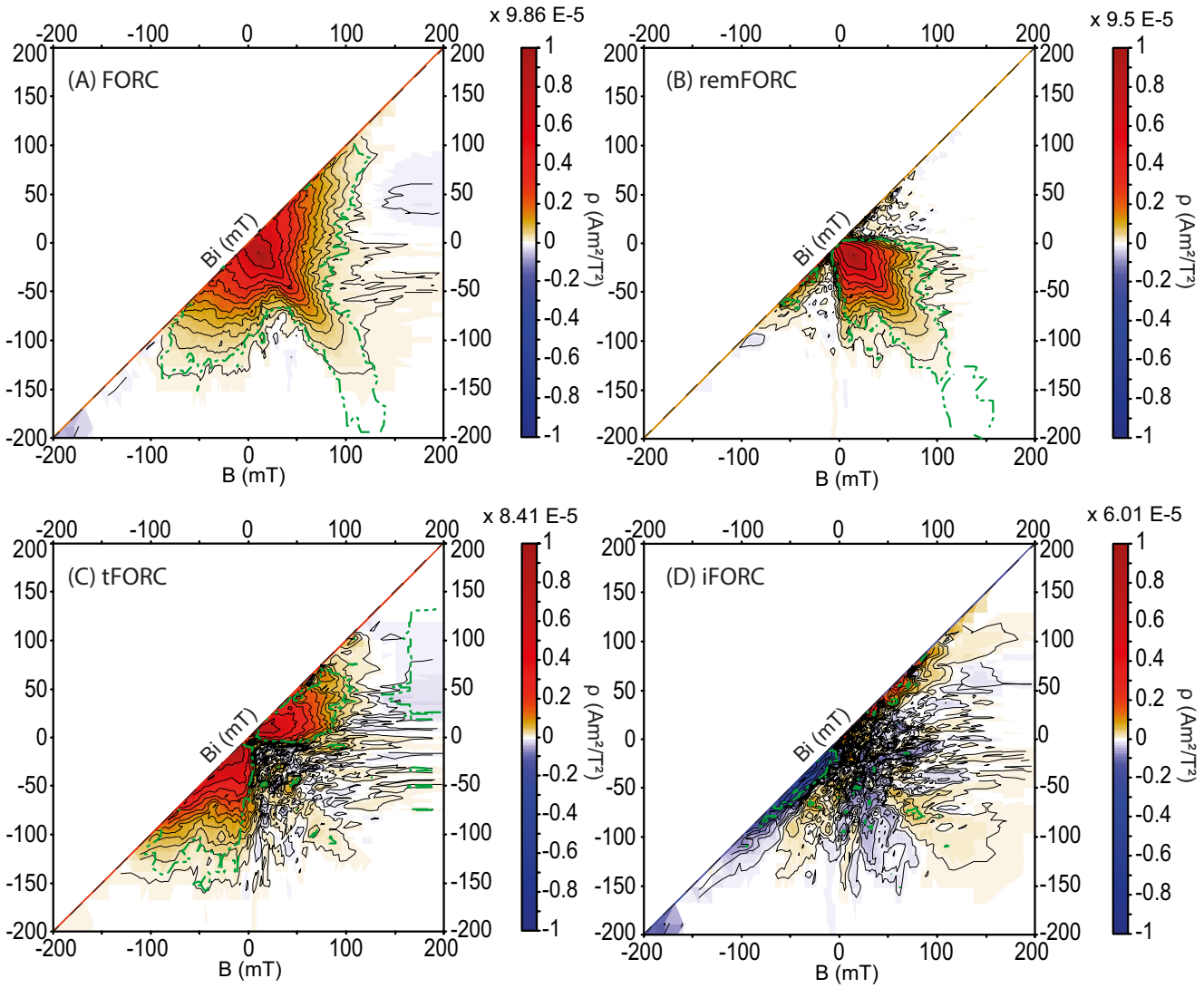

Figure 6. First-order reversal curve (FORC)-type diagrams for Sample 370-C0023A-93R-6W, 48–50 cm (depth: 962.99 meters below seafloor) in Magnetic Zone 4. (a) Conventional FORC diagram, (b) remanent FORC (remFORC) diagram, (c) transient hysteresis FORC (tFORC) diagram, and (d) induced FORC (iFORC) diagram. Green contours indicate the 0.05 significance level for the FORC distributions calculated according to Heslop and Roberts (2012). Complementary rock magnetic data discussed in the text for this sample are shown in Figure S7 in Supporting Information S1.

in Supporting Information S2). MZ 1 (from ~207 to ~498 mbsf) has the highest NRM, χ_{lf}, ARM, and SIRM values (core gap between 318.5 and 353 mbsf) and corresponds roughly to Lithologic Subunits IIA, IIB, and IIC (Figure 2; Heuer, Inagaki, Morono, Kubo, Maeda, Bowden, et al., 2017). MZ 2 (from ~500 to ~704 mbsf) has lower values of these magnetic parameters. MZ 2' (from ~621 to ~684 mbsf), within MZ 2, has slightly higher values compared to adjacent samples. MZ 3 (from ~719.4 to ~885 mbsf) has higher magnetic mineral concentrations. MZ 4 (from ~890.5 to ~1,099 mbsf) has the lowest values. Below MZ 1, down-core rock magnetic variations do not appear to correlate with lithological units. This is evident in Lithologic Unit IV, which includes MZs 3 and 4, which have higher and lower magnetic mineral concentrations, respectively (Figure 2). The MZs are described further below.

Lower concentration-dependent magnetic parameters could partially reflect dilution by increased carbonate ($CaCO_3$) contents. At Site C0023, $CaCO_3$ contents are generally scattered with an average of ~3.4 wt% and vary between 0.07 and 21.6 wt% (Figure S2 in Supporting Information S1; Heuer, Inagaki, Morono, Kubo, Maeda, Bowden, et al., 2017). Higher $CaCO_3$ values coincide with calcite veins and cements (Heuer, Inagaki, Morono, Kubo, Maeda, Bowden, et al., 2017). In the studied interval, ferrimagnetic mineral con-

centrations can only be diluted by a factor of 1.2 at maximum (dilution factor = $(100-CaCO_{3min})/(100-CaCO_{3max})$ where $CaCO_{3min}$ = 0.1 and $CaCO_{3max}$ = 16.5 are the minimum and maximum $CaCO_3$ contents (wt%), respectively; Heuer, Inagaki, Morono, Kubo, Maeda, Bowden, et al., 2017). Therefore, carbonate dilution alone cannot explain the order of magnitude NRM, ARM, and SIRM decrease between MZs 1 and 2, and between MZs 3 and 4. Grain size parameters, ARM/χ_{lf} and ARM/SIRM, behave differently down-core (Figure 2). ARM/χ_{lf} mirrors ARM variations and suggests the presence of finer magnetic grains in MZs 1 and 3. Lu and Banerjee (1994) suggested use of ARM/SIRM at nearby Site 808 because it is less sensitive to paramagnetism. Higher ARM/SIRM values suggest the presence of finer magnetic grains at the top of MZ 2, in MZ 3, and in a small interval within MZ 4. As discussed below, a mixture of magnetic minerals with different compositions, and in low concentrations in some intervals, challenge interpretation of these two ratios as magnetic grain size proxies.

3.1. Magnetic Zone 1 (~207 to ~498 mbsf)

MZ 1 corresponds to Lithologic Subunits IIA, IIB, IIC, and the top of Unit III. NRM, χ_{lf}, ARM, and SIRM are higher in MZ 1 compared to underlying sediments. These parameters are highest in Subunit IIA and indicate a higher magnetic mineral concentration, with high SIRM values in Subunit IIA due to the presence of high coercivity ferrimagnetic iron sulfides as shown below. $S_{-0.1T}$ is as low as 0.7 and B_{cr} is ~60 mT in Subunit IIA with lower values (<40 mT) likely corresponding to iron oxides (Figure 2).

Thermomagnetic curves indicate a mixture of magnetic minerals. Slope breaks at ~300–350°C, ~560°C, and ~650°C correspond, respectively, to thermal alteration of ferrimagnetic iron sulfides (greigite and/or pyrrhotite) and to Curie/Néel temperatures of (titano-)magnetite and hematite (Dunlop & Özdemir, 1997) (Figures S3a and S3e in Supporting Information S1). Hematite could be either detrital or a result of magnetite alteration during heating (van Velzen & Zijderveld, 1992). Ferrimagnetic iron sulfides are only present in higher coercivity samples (i.e., with B_{cr} >40 mT).

Low-temperature magnetic measurements cannot discriminate the presence of greigite because it does not have a low-temperature magnetic transition (Chang et al., 2009; Roberts et al., 2011). A transition is evident in RT-SIRM, ZFC, and FC curves at ~115 K, which is close to the Verwey transition temperature in magnetite (T_V = 120 K) (e.g., Muxworthy & McClelland, 2000; Özdemir et al., 2002) (Figures S3c, S3d, S3g and S3h in Supporting Information S1). The RT-SIRM curve is not reversible through T_V, which suggests the presence of single vortex (SV) to multidomain (MD) (titano-)magnetite (Özdemir et al., 2002). Selected samples have a clear Besnus transition due to monoclinic (4C) pyrrhotite at ~35 K (Besnus & Meyer, 1964; Dekkers et al., 1989; Rochette et al., 1990).

Conventional FORC diagrams either have closed contours with a 50–70 mT peak coercivity (Figure S3b in Supporting Information S1), which is typical of interacting single-domain (SD) greigite (e.g., Roberts et al., 2006, 2011), or triangular contours with peak coercivity at ~10–20 mT (Figure S3f in Supporting Information S1), which suggest the occurrence of vortex state iron oxides (e.g., Lascu et al., 2018; Muxworthy & Dunlop, 2002; Roberts et al., 2000, 2017). A few FORC diagrams have kidney-shaped contours typical of SD 4C (Wehland et al., 2005) or 3C pyrrhotite (Horng, 2018). To better characterize the domain states of magnetic minerals, additional FORC-type diagrams were measured for a subset of samples from MZ 1. Conventional FORC diagrams confirm the presence of SD greigite (Figure 3a). The positive region along the negative B_i axis in remFORC diagrams suggests the presence of viscous SP/SD particles (Zhao et al., 2017; Figure 3b). Two "wings" along the B_u axis with low coercivity peaks are present in tFORC diagrams (Figure 3c), which are typical of SV grains (Roberts et al., 2017; Zhao et al., 2017) or interacting SD particles (Harrison et al., 2018). Such grains are not evident in conventional FORC diagrams for sister samples (e.g., Figure S3b in Supporting Information S1), possibly because their contribution is lower than that of SD greigite. The negative-positive-negative pattern in the iFORC diagram (Figure 3d) indicates the presence of SD particles. A few samples from the bottom of MZ 1 have triangular FORC diagrams with low coercivity peaks (10–20 mT) and no evidence of ferrimagnetic iron sulfides (Figure S4 in Supporting Information S1). The iFORC diagram has two adjacent patterns: a negative-positive-negative response due to SD particles and a negative-positive-negative-positive response due to SV particles (Figure S4 in Supporting Information S1). Other rock magnetic results suggest that these grains are iron oxides (Figure S3 in Supporting Information S1).

3.2. Magnetic Zone 2 (~500 to ~704 mbsf)

NRM, χ_{lf}, ARM, and SIRM are lower in MZ 2 by about an order of magnitude compared to MZ 1 (Table S1 in Supporting Information S2), which suggests a lower magnetic mineral concentration. In this zone, χ_{fd}% is higher compared to adjacent zones by a factor of 5–10 (Figure 2). This indicates that smaller SP/SD particles are more abundant, especially in upper MZ 2 (~500 to ~620 mbsf), which corresponds roughly to Lithologic Unit III. Ash layers are abundant in this interval (Heuer, Inagaki, Morono, Kubo, Maeda, Bowden, et al., 2017), and the SP/SD grains likely come from disseminated volcanic ashes, even though discrete ash layers were avoided during sampling.

Magnetic measurements indicate a simpler magnetic mineral assemblage compared to that of MZ 1, which is composed mainly of low coercivity minerals. Thermomagnetic results (Figure S5a in Supporting Information S1) have a slope break at ~570–575°C, which is indicative of magnetite, and at ~650°C, which is indicative of hematite. By contrast to MZ 1, no slope break is observed at 300–350°C. Low-temperature magnetic measurements (Figures S5c and S5d in Supporting Information S1) have a marked irreversible Verwey transition, which supports the presence of magnetite. All measured conventional FORC diagrams have triangular contours with peak coercivity <20–30 mT (Figure S5b in Supporting Information S1), which is characteristic of vortex state magnetic grains (e.g., Lascu et al., 2018; Roberts et al., 2017). FORC and tFORC diagrams have low coercivity SV magnetic minerals with typical wing-shaped contours (Figures 4a and 4c) and a noisy negative-positive-negative-positive iFORC pattern (Figure 4d). Non-interacting SD particles with higher coercivities may be present, as indicated by a tail along the B_c axis. A remFORC diagram has a positive region on the negative B_i axis that indicates thermal activation of particles near the SP/SD threshold size (Figure 4b), which is consistent with higher χ_{fd}% values (Figure 2).

Within MZ 2, a thin interval (~621 to ~684 mbsf) has slightly higher NRM, ARM, χ_{lf}, and SIRM values (Figure 2), which suggest higher magnetic mineral concentrations. This zone was defined as MZ 2' in nearby sites (Shipboard Scientific Party, 1991, 2001). In this zone, χ_{fd}% decreases, which indicates less abundant SP particles (Figure 2). The magnetic mineralogy in MZ 2' is not different from that of MZ 2 with vortex state magnetite and hematite present. However, the average coercivity is slightly different between MZs 2 and 2'. The former has a larger higher coercivity mineral contribution. $S_{-0.1T}$ and $S_{-0.3T}$ are lower and the average B_{cr} value is ~36 mT in MZ 2 (compared to ~29 mT in MZ 2') (Table S2 in Supporting Information S2).

3.3. Magnetic Zone 3 (~719.4 to ~885 mbsf)

MZ 3 lies within Lithologic Unit IV and has higher NRM, ARM, χ_{lf}, and SIRM compared to MZs 2 and 4 (Figure 2). These parameters have lower average values (Table S1 in Supporting Information S2) than in MZ 1, except for ARM, which is higher in MZ 3 compared to MZ 1 and is nearly one order of magnitude higher than NRM, which suggests the occurrence of SD grains. These parameters have slightly lower values in the décollement zone (Figure 2) where the mean B_{cr} is ~32 mT, which is higher than in MZs 2' and 4 (Table S2 in Supporting Information S2).

Thermomagnetic measurements (Figure S6a in Supporting Information S1) indicate a mixture of titanomagnetite (T_C ~465–470°C), magnetite (T_C ~560°C), and hematite (T_N~620–650°C) in MZ 3. The Curie/Néel temperatures of magnetite and hematite are slightly lower than expected, which suggests that they are non-stoichiometric. Titanomagnetite and hematite are not always indicated in high temperature measurements. Low-temperature magnetization curves contain, similar to the intervals above, a well-marked Verwey transition (Figures S6c and S6d in Supporting Information S1), with two shoulders at ~100 and ~120 K, as seen in first derivatives of ZFC and FC curves (Figure S6d in Supporting Information S1). This suggests the presence of two (titano)-magnetite populations with different stoichiometry or grain size rather than a mixture of biogenic or detrital magnetite (Chang et al., 2016). Conventional FORC diagrams (Figure S6b in Supporting Information S1) are similar to those for MZ 2, with triangular-shaped contours and mean coercivity <20–30 mT. However, interactions among magnetic particles are slightly stronger in samples from MZ 3, which likely indicates a higher SD particle contribution. FORC and tFORC diagrams are typical of low coercivity vortex state minerals (Figures 5a and 5c), which is supported by a negative-positive-nega-

tive-positive iFORC pattern (Figure 5d). Non-interacting SD particles with higher coercivities are present, as indicated by a marked tail along the B_c axis, compared to MZ 2 (Figure 4a). A remFORC diagram contains a strong signal due to thermal activation in viscous SP/SD particles (Figure 5b), as characterized by the positive region along the negative B_i axis, compared to MZ 2 (Figure 4b).

MZ 3 includes the décollement zone (758.15–796.4 mbsf) with alternating meter-thick intact intervals and thinner fault zones (Heuer, Inagaki, Morono, Kubo, Maeda, Bowden, et al., 2017). In the décollement zone, ARM, χ_{lf}, and SIRM are lower than in adjacent areas (Figure 2). However, the coercivity (Figure 2) and magnetic mineral assemblage identified from low and high temperature measurements and FORC diagrams are not different from the rest of MZ 3.

3.4. Magnetic Zone 4 (~890.5 to ~1,099 mbsf)

MZ 4 occurs in the lower half of Lithologic Unit IV. NRM, χ_{lf}, ARM, and SIRM are the lowest on average compared to overlying MZs (Table S1 in Supporting Information S2), which indicate lower magnetic mineral contents. Magnetic parameters do not vary much in this interval, except for a 50-m thick interval (~1,000–1,050 mbsf) where ARM/SIRM, M_{rs}/M_s, and B_{cr} are higher and coercivity ratios lower (Figure 2). Magnetic results for samples from MZ 4 are similar to those from MZ 2. Thermomagnetic, low-temperature, and conventional FORC results are comparable (Figure S7 in Supporting Information S1) and the main identified magnetic phases are coarse vortex state magnetite and hematite. FORC diagrams are identical and indicate the presence of low coercivity vortex state particles, probable viscous particles near the SP/SD threshold size, and a higher coercivity magnetic phase (Figure 6). Overall, MZ 4 is similar to MZ 2 and differs only by having a lower magnetic mineral concentration.

3.5. Magnetic Mineral Assemblages at Site C0023: Summary

To summarize, the magnetic mineral assemblage at Site C0023 is dominated by vortex state (titano-)magnetite, which is found in all MZs (Figure S8 in Supporting Information S1). Weakly interacting higher coercivity grains are also present in all zones, which could be detrital SD hematite (identified by its Néel/Curie temperature in thermomagnetic curves). Iron oxides at Site C0023 are mainly detrital and are present in the four MZs with varying grain sizes and concentrations (Figure S9 in Supporting Information S1). MZ 1 is the only zone that contains authigenic ferrimagnetic iron sulfides. MZs 2 and 4 have similar magnetic mineral assemblages, with low vortex state (titano-)magnetite concentrations as indicated by down-core concentration-dependent parameter variations (Figure 2). Dia- and para-magnetic contributions are high (>60%) in MZs 2 and 4 (Figure S8 in Supporting Information S1), while ferrimagnetic contributions are higher in MZs 1 and 3.

4. Discussion

Magnetic mineral assemblages at Site C0023 vary with depth to define four main MZs. This zonation cannot only be explained by depositional processes because the lithologic units, which represent specific depositional episodes and/or sediment provenance changes (Heuer, Inagaki, Morono, Kubo, Maeda, & the Expedition 370 Scientists, 2017), do not always correspond to the MZs. The overall sediment composition (sediment type, grain size, $CaCO_3$ content) does not vary significantly among the four MZs (Figure S10 in Supporting Information S1). However, sedimentation rates (Hagino & the Expedition 370 Scientists, 2018) and organic matter contents (Figure S2 in Supporting Information S1; Heuer, Inagaki, Morono, Kubo, Maeda, Bowden, et al., 2017) vary at Site C0023 and control mainly the extent of diagenetic alteration of magnetic mineral assemblages. Diagenetic processes at Site C0023 have been reconstructed by Köster et al. (2021a) based on sedimentary Fe pool analysis. In the following, we discuss the rock magnetism of Site C0023 along with the findings of Köster et al. (2021a) and propose a burial diagenetic magnetic model for this site (Figures 7 and 8). Figure 8 gathers key information on the timing of key diagenetic events for the different formations, and stability fields for key iron minerals.

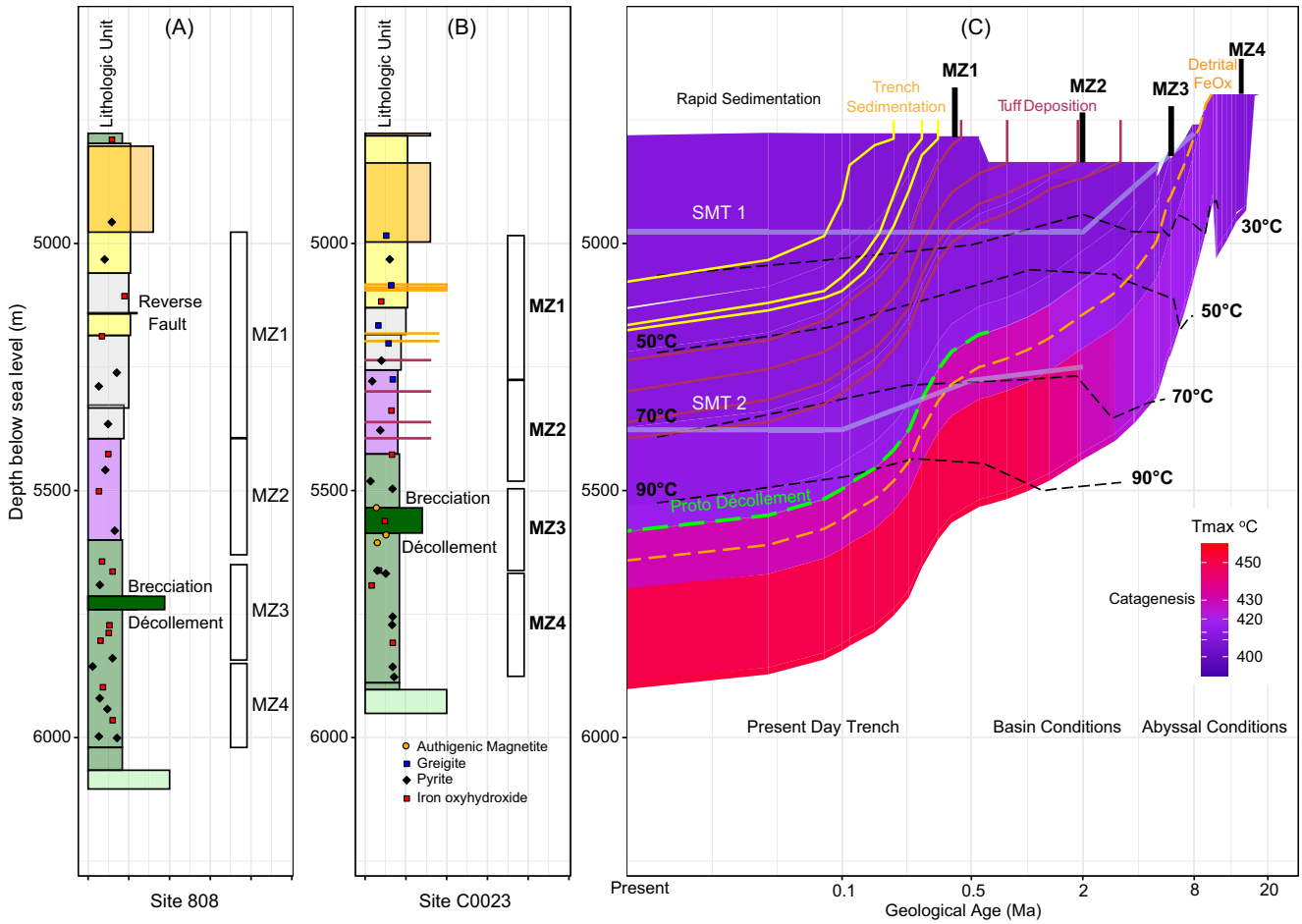

Figure 7. Lithological logs for (a) Sites 808 (Shipboard Scientific Party, 1991) and (b) C0023 (Heuer, Inagaki, Morono, Kubo, Maeda, & the Expedition 370 Scientists, 2017), with (c) illustration of the burial history at C0023 and key events. The color code for lithologic units and décollement is from Heuer, Inagaki, Morono, Kubo, Maeda, and the Expedition 370 Scientists (2017). Magnetic zones (MZs) and associated main magnetic minerals (represented by different symbols) at Sites 808 (Lu & Banerjee, 1994) and C0023 (this study) are indicated. See also Figure S11 in Supporting Information S1 for magnetic correlation between sites. T_{max} is the RockEval parameter and T_{max} ~ 435°C indicates the onset of catagenesis. The two sulfate-methane transitions (SMTs; Köster et al., 2021a) discussed in the text are reported. Time is indicated on a log scale to illustrate recent events and consequent processes (<0.5 Ma) that control diagenetic processes. Points used to construct Figure 8 are identified.

4.1. Depositional Environment and SMT Zones

Site C0023 experienced depositional environment changes during its tectonic displacement from the Shikoku Basin to the Nankai Trough. This was accompanied by burial temperature and resulting (bio-)geochemical process changes (Horsfield et al., 2006; Köster et al., 2021a; Tsang et al., 2020). The Lower Shikoku Basin facies (Lithologic Unit IV ~637–1,112 mbsf; 13.53–2.53 Ma) was deposited in an organic carbon-starved, low sedimentation abyssal environment (Köster et al., 2021a). Aerobic conditions prevented reductive dissolution and favored detrital magnetic mineral preservation, mainly iron (oxyhydr)oxides (Figures 7 and 8). As Site C0023 moved toward the Japanese island arc, sedimentation rates and organic carbon supply increased, leading to organoclastic iron and sulfate reduction as well as biogenic methanogenesis, and, thus, to anoxic depositional conditions for the Upper Shikoku Basin facies (Unit III at ~494–637 mbsf; 2.43–0.43 Ma, Köster et al., 2021a) (Figures 7 and 8). Following the onset of methanogenesis, sulfate diffusing down from the overlying seawater reacted with biogenic methane during AOM and a shallow SMT formed (Köster et al., 2021a). Therefore, most of the Upper Shikoku Basin facies was buried beneath a SMT by ~2 Ma (SMT 1 in Figures 7 and 8). Downward diffusing methane (from shallow SMT 1) reacted with residual upward diffusing sulfate in Unit IV to form a second, reverse SMT (SMT 2 in Figures 7 and 8; Köster et al., 2021a). Iron

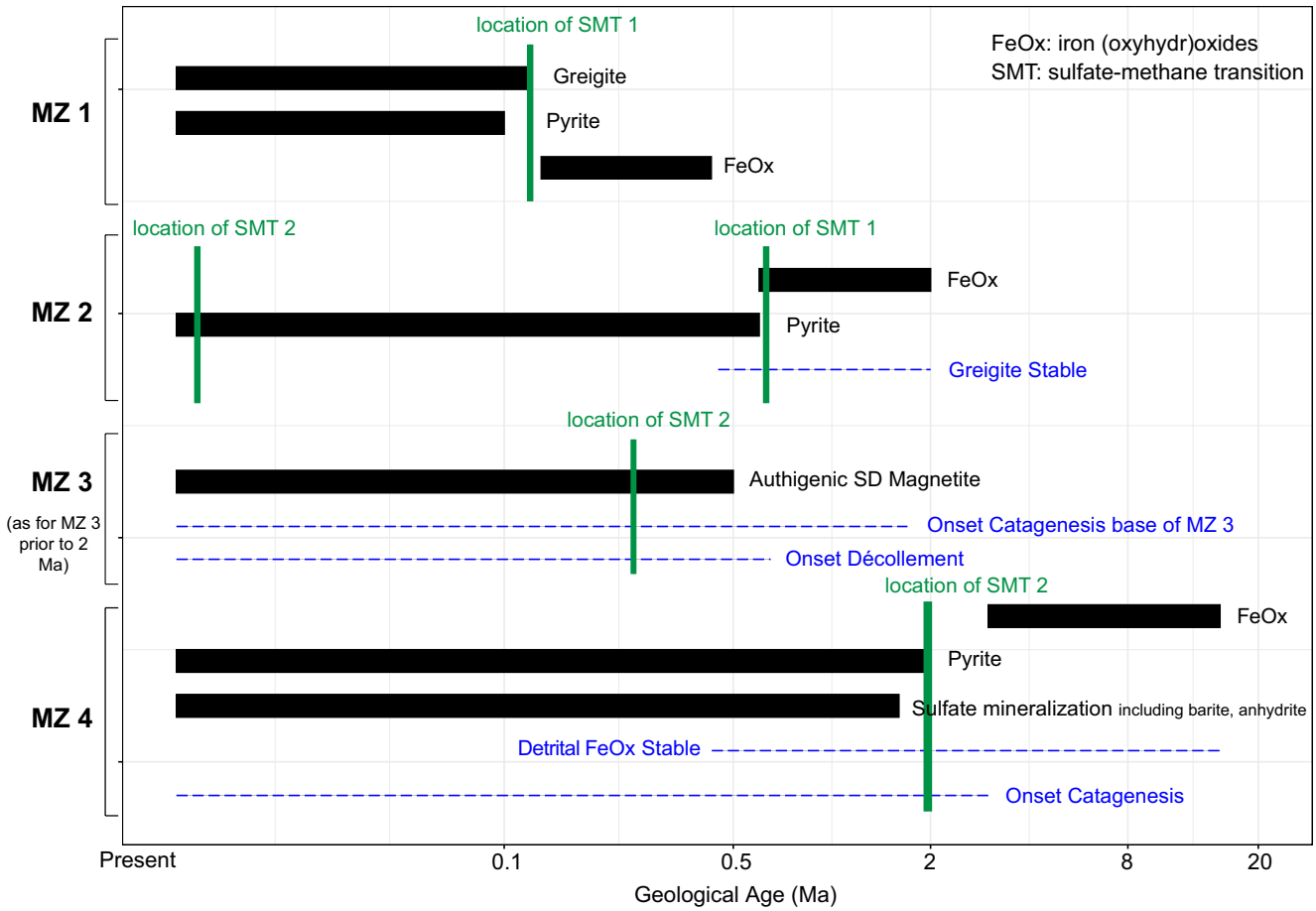

Figure 8. Paragenesis proposed from basin analysis (Tsang et al., 2020 and Figure 7) and magnetic mineral assemblage diagenetic histories discussed here and by Köster et al. (2021a). Separate paragenetic sequences are inferred for magnetic zones (MZs) 1 to 4, with a typical history indicated for the mid-point of each zone. Solid black bars indicate the main mineral phases for each MZ (Tsang et al., 2020). The dashed blue lines indicate stability fields for key iron minerals and the onset of other geological processes such as catagenesis. For example, it can be seen that MZ 2 (containing iron oxides) passes sulfate-methane transition (SMT) 1 (vertical green line) early at ~0.6 Ma, but most pyrite formation occurs much later (<0.5 Ma). Based on the rate and depth of burial, greigite is inferred to have been stable until ~0.5 Ma (blue dashed line). MZ 4 would not have passed through a SMT until more than 5 million years after its deposition, with the formation of iron oxyhydroxides (FeOx) favored prior to this. Time is indicated on a logarithmic scale as for Figure 7.

(oxyhydr)oxides were reduced by hydrogen sulfide produced during AOM to form iron sulfides (pyrite). The onset of SMT 2 coincided with the onset of catagenesis at 2 Ma in MZ 3 (Figures 7 and 8). Methane in SMT 2 is, thus, partly produced during catagenesis because Unit IV has generated thermogenic methane since 2 Ma (Figure 7). At SMT 2, methane and sulfate were consumed, and dissolved sulfide was released into porewater. This led to deep reductive iron dissolution in Unit IV with alteration of original magnetic mineral assemblages and pyrite formation occurring several million years after deposition (Köster et al., 2021a). At ~0.5 Ma, Site C0023 reached the Nankai Trough and the sedimentary and depositional environment changed to trench-deposited formations (Units IIA-IIC) that favored rapid burial below the shallow SMT with authigenic greigite preservation (Figure 7). About half of the sediment cover was deposited in <10% of the site history (Figure 7).

The presence of two SMTs can explain the nature of the magnetic mineral assemblages in MZs 2 and 4, that is, few preserved detrital ferrimagnetic minerals with authigenic pyrite formed from post-depositional reductive dissolution (Figure 8). However, it does not satisfactorily explain MZ 3. The present-day deep reverse SMT (between 640 and 764 mbsf) occurs in lowermost MZ 2 (including MZ 2') and upper MZ 3. Despite MZs 2 and 3 both being similarly situated with respect to SMT 2, they have contrasting magnetization and magnetic mineral assemblages.

Between ~400 and 600 mbsf, Fe^{2+} release coincides with abundant ash layers (Figures 7 and S2 in Supporting Information S1) where dissolved silica ($Si[OH]_4$) averages about 500 μM (Heuer, Inagaki, Morono, Kubo, Maeda, Bowden, et al., 2017). Magnetite is unstable under elevated porewater silica concentrations, such as those around abundant silicic volcanic ashes, and will dissolve rapidly to produce Fe-bearing smectite (Florindo et al., 2003). The dissolved silica concentration at Site C0023 is lower than in silica-rich sediments in which magnetite dissolution has been reported (Florindo et al., 2003). Although (abiotic) silicate weathering could partly explain Fe^{2+} release (e.g., Luo et al., 2020), this is not the main mechanism that explains low magnetic susceptibility values in MZ 2. Therefore, it is reasonable to consider potential biogeochemical processes in MZs 2 and 3. DNA-based community analyses for samples below ~320 mbsf are not informative because of low vegetative cell concentrations, and no cells or endospores are detectable between 840 and 1,100 mbsf, that is, in MZ 4 (Heuer et al., 2020). The current depth of the lower reverse SMT has a temperature of ~85°C (Heuer et al., 2020), which is the "cut-off" temperature for microbial life in the surface of deep petroleum reservoirs (Head et al., 2003) and in the hot Guaymas Basin (McKay et al., 2016). However, microorganisms can still be active at this temperature (Holler et al., 2011; Kallmeyer & Boetius, 2004), so microbial processes need not be ruled out based on this temperature threshold alone. If present-day AOM reactions are active in the deep reverse SMT, they probably have extremely low rates (Köster et al., 2021a), and are unlikely to explain magnetic mineral assemblage differences between MZs 2 and 3. Subsurface temperatures at C0023 were also higher in the near past (Horsfield et al., 2006; Tsang et al., 2020), so both MZs have been heated to temperatures near the "cut-off" for life in petroleum reservoirs (Figure 7).

4.2. Greigite Formation and Preservation

MZ 1 differs from the three other MZs because it contains ferrimagnetic iron sulfides. Greigite can form authigenically by different pathways either biotically or abiotically (Roberts, 2015; and references therein). Under steady state conditions, greigite eventually transforms into pyrite. The presence of greigite down to ~460 mbsf at Site C0023 suggests that in situ conditions favored its preservation and inhibition of pyritization, that is, by low availability of dissolved sulfide H_2S/HS^-. Sulfate (SO_4^{2-}) and H_2S/HS^- concentrations are low or below detection limits down to at least ~550 mbsf (Figure S2 in Supporting Information S1; Heuer, Inagaki, Morono, Kubo, Maeda, Bowden, et al., 2017), which favors greigite preservation (Kao et al., 2004). Shallow sediment was not drilled during IODP Expedition 370, so no information on a shallow SMT is available at Site C0023. Nevertheless, at nearby ODP Site 1174, a shallow SMT is identified below 5 mbsf (Shipboard Scientific Party, 2001), so we assume that it also occurs at Site C0023. Authigenic greigite was preserved as a microbial by-product during burial under anoxic conditions. *Atribacteria* occur above 254 mbsf at Site C0023 (Heuer, Inagaki, Morono, Kubo, Maeda, Bowden, et al., 2017), which provides a further indication of organic-rich anoxic (Reed et al., 2002). Greigite preservation can occur because of high sedimentation rates (>600 m/Myr for <473 mbsf; Hagino & the Expedition 370 Scientists, 2018). Rapid burial of Units IIC-IIA through the shallow SMT gives insufficient time for full pyritization of greigite that formed ~0.5 Ma ago (Köster et al., 2021a; contrast between MZs 1 and 2 in Figure 8).

4.3. Role of Burial Temperature and Fluids

Whereas (titano-)magnetite is ubiquitous at Site C0023 and is present in all MZs, MZ 3 (~720–885 mbsf) has an additional fine-grained magnetic phase. Larger ARMs (Figure 2) and two shoulders on derivatives of ZFC and FC curves (Figure S6 in Supporting Information S1) suggest the presence of SD magnetite, which is also supported by the IRM unmixing results of Köster et al. (2021a, 2021b). Three main hypotheses are suggested to explain the presence of authigenic fine-grained magnetite in MZ 3: (a) a burial temperature increase that may or may not be associated with hydrocarbon generation, (b) fluid circulation, (c) microbial iron reduction, or a combination of these hypotheses, as discussed further here.

1. Present-day heat flow at Site C0023 is 140 mW/m^2, with an average geothermal gradient of 111°C/km (Heuer et al., 2020; Heuer, Inagaki, Morono, Kubo, Maeda, Bowden, et al., 2017). This converts to downhole temperatures of ~32–62°C, ~62–82°C, ~82–97°C, and ~97–114°C for MZs 1, 2, 3, and 4, respectively. Laboratory heating of sediments indicates that new magnetic minerals, such as magnetite, can form under the sole effect of increased temperature (e.g., Aubourg & Pozzi, 2010; Aubourg et al., 2008; Kars

et al., 2012). Temperatures as low as 50°C are sufficient to form new magnetic minerals (Kars et al., 2012). Hydrocarbon generation deeper in the sediment (e.g., Abubakar et al., 2015; Badejo et al., 2021; Elmore et al., 1987; McCabe et al., 1987) and tectonic fluid circulation (e.g., Elmore et al., 2001; McCabe et al., 1989) can lead to abiotic magnetic mineral formation and/or to alteration of pre-existing magnetic minerals. Rock-Eval pyrolysis measurements were carried out to further investigate potential effects of progressive increases in temperature, magnetic mineral content, and catagenesis (high temperature organic matter decomposition). T_{max} varies between 349 and 450°C in the ~190–1,177 mbsf interval (average: 430 ± 12°C; Figure S10 in Supporting Information S1) (Stein, 2021). T_{max} is above 435°C below 800 mbsf (i.e., below the décollement), which represents the boundary between immature and mature organic matter (Tissot et al., 1987). Basin modeling also suggests that the lower part of Lithologic Unit IV below the décollement has been heated sufficiently by burial diagenesis to generate hydrocarbons since 2 Ma for the lower part of the Lower Shikoku Basin facies (Tsang et al., 2020; Figures 7 and 8). Heuer et al. (2020) reported that methane occurs with other hydrocarbons (ethane, propane, butane) at Site C0023, which were likely generated by catagenesis (Heuer et al., 2020; Heuer, Inagaki, Morono, Kubo, Maeda, Bowden, et al., 2017). Below ~800 mbsf, MZs 3 and 4 have distinct magnetic mineral assemblages and contrasting magnetic properties (Figure 2). MZ 4 and parts of MZ 3 have undergone catagenesis for comparable lengths of time (Figures 7 and 8), so it is unlikely that magnetite in MZ 3 is solely related to hydrocarbon generation or MZ 4 would have similar magnetite contents.

2. Sediments underthrust below the décollement and above basement (at 775–1,121 mbsf) host hydrothermal barite ($BaSO_4$) and rhodochrosite ($MnCO_3$) that precipitated in stratabound patches and veins (Tsang et al., 2020; Figure 8). Time-limited and repeated hydrothermal fluid ingression (~140–220°C) occurred in the underthrust sediments where short-term, localized heating may have occurred within the fracture zone (~200°C for less than a year) (Tsang et al., 2020). It is, thus, reasonable to propose that thrust faults above and faulting below the décollement (Heuer, Inagaki, Morono, Kubo, Maeda, Bowden, et al., 2017) facilitated fluid circulation to promote fine-grained magnetite formation in MZ 3. Authigenic magnetite could have formed from smectite-derived iron during diagenetic illitization triggered by potassium-rich brines (e.g., McCabe et al., 1989). By contrast to Lithologic Unit III (494–673.25 mbsf), which includes MZ 2 and where major tuff layers are observed, Unit IV, which includes MZ 3, consists of 97% mudstone (Heuer, Inagaki, Morono, Kubo, Maeda, Bowden, et al., 2017). MZ 3 (720–890 mbsf) is characterized by downward decreasing smectite contents from 80 (at ~600 mbsf) to 20 wt% (at ~850 mbsf) in association with progressive illitization (Kim et al., 2019). However, porewater K^+ is low (<1 mM) in this interval (Heuer, Inagaki, Morono, Kubo, Maeda, Bowden, et al., 2017; Kim et al., 2019), although this is the present-day situation, and might not have been the case during episodic short-term pulses of hydrothermal fluids. Kim et al. (2019) suggested that thermogenic oxidative conditions exist below 700 mbsf and above 80°C to initiate abiotic illitization. Therefore, authigenic magnetite formation via hydrothermal fluid ingression is a plausible mechanism. Sediments in MZ 4 are more compacted, porosities are lower (Heuer, Inagaki, Morono, Kubo, Maeda, & the Expedition 370 Scientists, 2017), and faulting is generally associated with closed or mineralized faults. Thus, the two MZs, that is, MZs 3 and 4, today have contrasting hydrodynamic regimes, despite ultimately resulting from the same processes that formed the accretionary prism.
3. Microbial iron reduction in methanogenic environments is a further mechanism to explain SD authigenic magnetite in MZ 3. It has been proposed that under variable methane seepage intensities, secondary iron (oxyhydr)oxides formed from iron sulfide oxidation associated with downward percolating oxidizing fluids and then rapidly buried below a SMT, can act as electron acceptors to form microbially driven magnetite, although the magnetite formation mechanism is yet to be determined (Lin et al., 2021). It is possible that after ~0.5 Ma, with increased methanogenesis and sediment temperature (Köster et al., 2021a), iron (oxyhydr)oxide reduction in the sediment could have occurred concurrently with fault-related fluid circulation.

4.4. Comparison With ODP Sites 808 and 1174

The MZs at Site C0023 are defined based on NRM intensity as was the case for nearby ODP Sites 808 (Shipboard Scientific Party, 1991) and 1174 (Shipboard Scientific Party, 2001). The depth and thickness of MZs differ from each other at the three sites (Table S3 in Supporting Information S2, Figure S12 in Supporting

Information S1). Common features are: MZ 1 corresponds to all sedimentary facies in Unit II; MZ 2 (including MZ 2') corresponds to the lower Upper Shikoku Basin and upper Lower Shikoku Basin facies; MZ 3 includes the décollement zone at all three sites, and MZ 4 is within the Lower Shikoku Basin (Figure 8). The proximity of the three sites indicates that similar diagenetic processes are responsible for the observed magnetic mineral variations.

At Site 808, episodically enhanced non-steady state magnetite dissolution has been invoked to explain lower NRM intensities in some intervals (Lu & Banerjee, 1994). Variable sediment provenance and calcite dilution were ruled out as responsible for lower NRM intensities. Instead, catagenesis was proposed to be responsible for magnetite dissolution at Site 808 (Lu & Banerjee, 1994): CO_2 produced by catagenesis results in Fe^{3+} reduction, which causes magnetite dissolution. $CaCO_3$ contents and total sulfur (TS) are also higher in low intensity intervals (Lu & Banerjee, 1994). At Site C0023, $CaCO_3$ is not clearly higher in MZs 2 and 4 (Figure S2 in Supporting Information S1; Heuer, Inagaki, Morono, Kubo, Maeda, Bowden, et al., 2017). However, TS coincides with elevated chromium reducible sulfur (CRS), which suggests that Fe oxides were diagenetically converted into pyrite in the Lower Shikoku Basin facies (Köster et al., 2021a). The lower magnetic intensity in MZs 2 and 4 could be partly due to magnetite dissolution from catagenesis.

Higher hydrocarbon gas (e.g., butane and pentane) contents were detected at Site 808 (Taira et al., 1991) in low magnetic intensity intervals (Lu & Banerjee, 1994). Similar gas anomalies within the Upper and Lower Shikoku Basin facies occur at Site 1174 (Shipboard Scientific Party, 2001). At Site C0023, notable propane and *i*-butane increases are observed between 470 and 640 mbsf (corresponding roughly to MZ 2) and below the décollement (>900 mbsf) (Heuer, Inagaki, Morono, Kubo, Maeda, Bowden, et al., 2017). These anomalies were explained at Site 808 as due to combined upward thermogenic gas migration along faults and gas production from immature kerogen (U. Berner & Faber, 1993). Tsang et al. (2020) showed that organic matter in underthrust sediments reaches pre-oil window to early oil window thermal maturity with temperatures <120°C under the sole effect of burial diagenesis, which is consistent with Rock-Eval data (Figure S10 in Supporting Information S1; Stein, 2021). Higher burial paleotemperature are not expected in the low magnetic intensity zones based on basin modeling and thermal maturity proxies (Tsang et al., 2020), which rules out a higher degree of maturity in MZs 2 and 4. The onset of catagenesis with associated thermal maturity (T_{max}~435°C) is insufficient to catalyze reactions that produce SD magnetic minerals in petroleum rocks. From laboratory heating experiments, Aubourg et al. (2012) and Abubakar et al. (2015), amongst others, suggested that the peak temperature of magnetic minerals is ~200–250°C in source rocks. It remains challenging to extrapolate laboratory results to natural processes. These two studies focused only on abiotic processes and did not consider microbial activity, which also plays a role in magnetic mineral formation during oil biodegradation (Emmerton et al., 2013). Catagenesis, as proposed by Lu and Banerjee (1994) for Site 808, is likely not the main explanation for low magnetic intensities at Site C0023. At Site 808, the higher magnetic intensity zone (i.e., MZ 3 at Site C0023) between low intensity MZs 2 and 4 was explained either as an interval with better magnetite preservation because of less corrosive porewaters or as an interval where cold water circulates and prevents catagenesis, or as a combination of both (Lu & Banerjee, 1994). SD magnetite authigenesis in MZ 3 may be a better explanation for producing higher magnetizations between the two low magnetic intensity zones. No detailed magnetic study has been published for Site 1174, but similar diagenetic processes are expected to have acted because of the close geographical proximity and similar magnetic assemblages at Sites C0023 and 808 (Shipboard Scientific Party, 2001; Figures 8 and S12 in Supporting Information S1).

5. Conclusions

At Site C0023, four major MZs are identified based on down-core magnetic properties. MZs 2 and 4 contain few magnetic minerals, which are mainly coarse relict vortex state (titano-)magnetite that survived diagenetic dissolution. MZ 1 is a high magnetic intensity zone that contains greigite that formed as a by-product of microbial activity at a shallow SMT. Greigite is preserved because of high sedimentation rates. MZ 3 is another high magnetic intensity zone that contains authigenic fine-grained magnetite, although the process responsible for its presence is yet to be determined. Catagenesis, fluid circulation, ash alteration, and microbial iron reduction all affect magnetic mineral assemblages at Site C0023 to varying degrees. Processes such as catagenesis and elevated interstitial silica due to ash alteration would lead to magnetic mineral dissolution,

whereas fluid circulation could be responsible for mineral authigenesis. Microbial iron reduction is versatile and can contribute to both magnetic mineral formation and reduction. Diagenetic processes (early/late, biotic/abiotic) are important in active tectonic settings such as the Nankai accretionary prism. They can modify paleomagnetic records substantially by changing the primary magnetic mineral assemblage and by adding later formed authigenic magnetic minerals. Therefore, to correctly interpret the paleomagnetic record, it is essential to investigate possible overprinting due to diagenetic transformations. We demonstrate the importance of combining different magnetic techniques, that is, rapid bulk measurements and more time-consuming high-resolution magnetic measurements (irregular FORCs), to characterize complex magnetic mineral assemblages. Use of irregular FORCs brings key insights into the complex magnetic mineral assemblages at Site C0023. Our study was conducted more than 25+ years after that of Lu and Banerjee (1994) at Site 808 and indicates that diagenetic processes responsible for magnetic mineralogy variations are much more complex than only catagenesis, as initially proposed, with several mechanisms possibly acting at the same time. Assessing the types and extent of non-steady state diagenetic alteration and its impact on magnetic mineralogy is important in marine sediments to assess the reliability of paleomagnetic records, including possible remagnetizations, and for redox paleo-reconstructions to determine the relative sequence of biogeochemical conditions in the geologic record. Integrated multidisciplinary magnetic, geochemical, and microbial analyses are essential to better understand diagenetic processes.

Conflict of Interest

The authors declare no conflicts of interest relevant to this study.

Data Availability Statement

Shipboard data from IODP Expedition 370 are accessible at https://sio7.jamstec.go.jp. Expedition 370 Proceedings are available from https://publications.iodp.org/proceedings/370/370title.html. Additional relevant data and figures are provided in Supporting Information S1 or are archived in the World Data Center PANGAEA. Rock magnetic data are available at https://doi.pangaea.de/10.1594/PANGAEA.929380 (Kars & Köster, 2021) and thermal maturity data at https://doi.pangaea.de/10.1594/PANGAEA.936510 (Stein, 2021).

Acknowledgments
This research used samples and data provided by the International Ocean Discovery Program (IODP). The authors thank the Marine Works Japan staff at the Kochi Core Center for support during sampling. This work was supported by the Japan Society for the Promotion of Science Grant-in-Aid for Science Research (grant 17K05681 to Myriam Kars), the German Research Foundation (DFG grants 388260220 to Male Köster and Susann Henkel, and 408178672 to Florence Schubotz), and the Australian Research Council (grant DP200100765 to Andrew P. Roberts). The authors also thank two anonymous reviewers for their constructive comments and Editor Joshua Feinberg for handling the manuscript.

References

Abubakar, R., Muxworthy, A. R., Sephton, M. A., Southern, P., Watson, J. S., Fraser, J. S., & Almeida, T. P. (2015). Formation of magnetic minerals at hydrocarbon-generation conditions. *Marine and Petroleum Geology*, *68*, 509–519. https://doi.org/10.1016/j.marpetgeo.2015.10.003

Aromokeye, D. A., Oni, O. E., Tebben, J., Yin, X., Richter-Heitmann, T., Wendt, J., et al. (2021). Crystalline iron oxides stimulate methanogenic benzoate degradation in marine sediment-derived enrichment cultures. *The ISME Journal*, *15*, 965–980. https://doi.org/10.1038/s41396-020-00824-7

Aubourg, C., & Pozzi, J.-P. (2010). Toward a new <250°C pyrrhotite–magnetite geothermometer for claystones. *Earth and Planetary Science Letters*, *294*, 47–57. https://doi.org/10.1016/j.epsl.2010.02.045

Aubourg, C., Pozzi, J. P., Janots, D., & Sahraoui, L. (2008). Imprinting chemical remanent magnetization in claystones at 95°C. *Earth and Planetary Science Letters*, *272*, 172–180. https://doi.org/10.1016/j.epsl.2008.04.038

Aubourg, C., Pozzi, J.-P., & Kars, M. (2012). Burial, claystones remagnetization and some consequences to magnetostratigraphy. In R. D. Elmore, A. R. Muxworthy, M. M. Aldana, & M. Mena (Eds.), *Remagnetization and chemical alteration of sedimentary rocks* (Vol. 371, pp. 181–188). Geological Society, London, Special Publication. https://doi.org/10.1144/SP371.4

Badejo, S. A., Muxworthy, A. R., Fraser, A., Neumaier, M., Perkins, J. R., Stevenson, G. R., & Davey, R. (2021). Using magnetic techniques to calibrate hydrocarbon migration in petroleum systems modelling: A case study from the Lower Tertiary, UK Central North Sea. *Geophysical Journal International*. https://doi.org/10.1093/gji/ggab236

Behar, F., Beaumont, V., & Penteado, H. L. D. B. (2001). Rock-Eval 6 technology: Performances and developments. *Oil & Gas Science and Technology IFP*, *56*, 111–134. https://doi.org/10.2516/ogst:2001013

Berner, R. A. (1981). A new geochemical classification of sedimentary environments. *Journal of Sedimentary Petrology*, *51*, 359–365. https://doi.org/10.1306/212f7c7f-2b24-11d7-8648000102c1865d

Berner, R. A. (1984). Sedimentary pyrite formation: An update. *Geochimica et Cosmochimica Acta*, *48*(4), 605–615. https://doi.org/10.1016/0016-7037(84)90089-9

Berner, U., & Faber, E. (1993). Light hydrocarbons in sediments of the Nankai accretionary prism (leg 131, site 808). In I. A. Hill, A. Taira, J. V. Firth & P. J. Vrolijk (Eds.), *Proceedings of the Ocean Drilling Program, scientific results* (Vol. 131, pp. 185–195). Ocean Drilling Program. https://doi.org/10.2973/odp.proc.sr.131.120.1993

Besnus, M. J., & Meyer, A. J. P. (1964). Nouvelles données expérimentales sur le magnétisme de la pyrrhotine naturelle. In *Proceedings of the International Conference on Magnetism* (Vol. 20, pp. 507–511). Institute of Physics.

Bloemendal, J., King, J. W., Hall, F. R., & Doh, S.-J. (1992). Rock magnetism of Late Neogene and Pleistocene deep-sea sediments: Relationship to sediment sources, diagenetic processes and sediment lithology. *Journal of Geophysical Research*, *97*(B4), 4361–4375. https://doi.org/10.1029/91JB03068

Canfield, D. E., & Berner, R. A. (1987). Dissolution and pyritization of magnetite in anoxic marine sediments. *Geochimica et Cosmochimica Acta*, *51*(3), 645–659. https://doi.org/10.1016/0016-7037(87)90076-7

Chang, L., Heslop, D., Roberts, A. P., Rey, D., & Mohamed, K. J. (2016). Discrimination of biogenic and detrital magnetite through a double Verwey transition temperature. *Journal of Geophysical Research: Solid Earth*, *121*, 3–14. https://doi.org/10.1002/2015JB012485

Chang, L., Roberts, A. P., Rowan, C. J., Tang, Y., Pruner, P., Chen, Q., & Horng, C.-S. (2009). Low-temperature magnetic properties of greigite (Fe_3S_4). *Geochemistry, Geophysics, Geosystems*, *10*, Q01Y04. https://doi.org/10.1029/2008GC002276

Dekkers, M. J., Mattéi, J. L., Fillion, G., & Rochette, P. (1989). Grain-size dependence of magnetic behavior of pyrrhotite during its low temperature transition at 34 K. *Geophysical Research Letters*, *16*(8), 855–858. https://doi.org/10.1029/GL016i008p00855

Dunlop, D. J., & Özdemir, Ö. (1997). *Rock magnetism: Fundamentals and frontiers* (p. 573). Cambridge University Press. https://doi.org/10.1017/CBO9780511612794

Elmore, R. D., Engel, M. H., Crawford, L., Nick, K., Imbus, S., & Sofer, Z. (1987). Evidence for a relationship between hydrocarbons and authigenic magnetite. *Nature*, *325*, 428–430. https://doi.org/10.1038/325428a0

Elmore, R. D., Kelley, J., Evans, M., & Lewchuk, M. (2001). Remagnetization and orogenic fluids: Testing the hypothesis in the Central Appalachians. *Geophysical Journal International*, *144*, 568–576. https://doi.org/10.1111/j.1365-246x.2001.00349.x

Emmerton, S., Muxworthy, A. R., Sephton, M. A., Aldana, M., Costanzo-Alvarez, V., Bayona, G., & Williams, W. (2013). Correlating biodegradation to magnetization in oil bearing sedimentary rocks. *Geochimica et Cosmochimica Acta*, *112*, 146–165. https://doi.org/10.1016/j.gca.2013.03.008

Espitalié, J., Laporte, J. L., Madec, M., Marquis, F., Leplat, P., Paulet, J., & Boutefeu, A. (1977). Méthode rapide de caractérisation des roches mères, de leur potentiel pétrolier et de leur degré d´évolution. *Revue de l'Institut Français du Petrole*, *32*, 23–42. https://doi.org/10.2516/ogst:1977002

Florindo, F., Roberts, A. P., & Palmer, M. R. (2003). Magnetite dissolution in siliceous sediments. *Geochemistry, Geophysics, Geosystems*, *4*(7), 1053. https://doi.org/10.1029/2003GC000516

Hagino, K., & the Expedition 370 Scientists. (2018). Data report: Calcareous nannofossils from the middle Miocene to Pleistocene, IODP Expedition 370 Site C0023. In V. B. Heuer, F. Inagaki, Y. Morono, Y. Kubo, L. Maeda (Eds.), & the Expedition 370 Scientists. (Eds.), *Temperature limit of the deep biosphere off Muroto* (Vol. 370). Proceedings of the International Ocean Discovery Program. https://doi.org/10.14379/iodp.proc.370.201.2018

Harrison, R. J., & Feinberg, J. M. (2008). FORCInel: An improved algorithm for calculating first order reversal curve distributions using locally weighted regression smoothing. *Geochemistry, Geophysics, Geosystems*, *9*, Q05016. https://doi.org/10.1029/2008GC001987

Harrison, R. J., Muraszko, J., Heslop, D., Lascu, I., Muxworthy, A. R., & Roberts, A. P. (2018). An improved algorithm for unmixing first-order reversal curve diagrams using principal component analysis. *Geochemistry, Geophysics, Geosystems*, *19*, 1595–1610. https://doi.org/10.1029/2018GC007511

Head, I. M., Jones, D. M., & Larter, S. R. (2003). Biological activity in the deep subsurface and the origin of heavy oil. *Nature*, *426*, 344–352. https://doi.org/10.1038/nature02134

Heslop, D., & Roberts, A. P. (2012). Estimation of significance levels and confidence intervals for first-order reversal curve distributions. *Geochemistry, Geophysics, Geosystems*, *13*, Q12Z40. https://doi.org/10.1029/2012GC004115

Heuer, V. B., Inagaki, F., Morono, Y., Kubo, Y., Maeda, L., Bowden, S., et al. (2017). Site C0023. In V. B. Heuer, F. Inagaki, Y. Morono, Y. Kubo, L. Maeda (Eds.), & the Expedition 370 Scientists. (Eds.), *Temperature limit of the deep biosphere off Muroto* (Vol. 370). Proceedings of the International Ocean Discovery Program. https://doi.org/10.14379/iodp.proc.370.103.2017

Heuer, V. B., Inagaki, F., Morono, Y., Kubo, Y., Maeda, L., & the Expedition 370 Scientists. (2017). Temperature limit of the deep biosphere off Muroto. In *Proceedings of the International Ocean Discovery Program* (Vol. 370). International Ocean Discovery Program. https://doi.org/10.14379/iodp.proc.370.2017

Heuer, V. B., Inagaki, F., Morono, Y., Kubo, Y., Spivack, A. J., Viehweger, B., et al. (2020). Temperature limits to deep subseafloor life in the Nankai Trough subduction zone. *Science*, *370*, 1230–1234. https://doi.org/10.1126/science.abd7934

Holler, T., Widdel, F., Knittel, K., Amann, R., Kellermann, M. Y., Hinrichs, K.-U., et al. (2011). Thermophilic anaerobic oxidation of methane by marine microbial consortia. *The ISME Journal*, *5*, 1946–1956. https://doi.org/10.1038/ismej.2011.77

Horng, C.-S. (2018). Unusual magnetic properties of sedimentary pyrrhotite in methane seepage sediments: Comparison with metamorphic pyrrhotite and sedimentary greigite. *Journal of Geophysical Research: Solid Earth*, *123*, 4601–4617. https://doi.org/10.1002/2017JB015262

Horsfield, B., Schenk, H. J., Zink, K., Ondrak, R., Dieckmann, V., Kallmeyer, J., et al. (2006). Living microbial ecosystems within the active zone of catagenesis: Implications for feeding the deep biosphere. *Earth and Planetary Science Letters*, *246*, 55–69. https://doi.org/10.1016/j.epsl.2006.03.040

Housen, B. A., & Musgrave, R. J. (1996). Rock-magnetic signature of gas hydrates in accretionary prism sediments. *Earth and Planetary Science Letters*, *139*(3–4), 509–519. https://doi.org/10.1016/0012-821X(95)00245-8

Jørgensen, B. B., Beulig, F., Egger, M., Petro, C., Scholze, C., & Røy, H. (2019). Organoclastic sulfate reduction in the sulfate-methane transition of marine sediments. *Geochimica et Cosmochimica Acta*, *254*, 231–245. https://doi.org/10.1016/j.gca.2019.03.016

Kallmeyer, J., & Boetius, A. (2004). Effects of temperature and pressure on sulfate reduction and anaerobic oxidation of methane in hydrothermal sediments of Guaymas Basin. *Applied and Environmental Microbiology*, *70*(2), 1231–1233. https://doi.org/10.1128/aem.70.2.1231-1233.2004

Kao, S.-J., Horng, C.-S., Roberts, A. P., & Liu, K.-K. (2004). Carbon-sulfur-iron relationships in sedimentary rocks from southwestern Taiwan: Influence of geochemical environment on greigite and pyrrhotite formation. *Chemical Geology*, *203*(1–2), 153–168. https://doi.org/10.1016/j.chemgeo.2003.09.007

Kars, M., Aubourg, C., Pozzi, J.-P., & Janots, D. (2012). Continuous production of nanosized magnetite through low grade burial. *Geochemistry, Geophysics, Geosystems*, *13*(8), Q08Z48. https://doi.org/10.1029/2012GC004104

Kars, M., & Kodama, K. (2015a). Rock magnetic characterization of ferrimagnetic iron sulfides in gas hydrate-bearing marine sediments at Site C0008, Nankai Trough, Pacific Ocean, off-coast Japan. *Earth, Planets and Space*, *67*, 18. https://doi.org/10.1186/s40623-015-0287-y

Kars, M., & Kodama, K. (2015b). Authigenesis of magnetic minerals in gas hydrate-bearing sediments in the Nankai Trough, offshore Japan. *Geochemistry, Geophysics, Geosystems*, *16*, 947–961. https://doi.org/10.1002/2014GC005614

Kars, M., & Köster, M. (2021). *Rock magnetic data of IODP Hole 370-C0023A*. PANGAEA. https://doi.org/10.1594/PANGAEA.929380

Kim, J., Dong, H., Yang, K., Park, H., Elliott, W. C., Spivack, A., et al. (2019). Naturally occurring, microbially induced smectite-to-illite reaction. *Geology*, *47*(6), 535–539. https://doi.org/10.1130/G46122.1

Kinoshita, M., Tobin, H., Ashi, J., Kimura, G., Lallement, S., Screaton, E. J., et al. (2009). *Proceedings of the Integrated Ocean Drilling Program* (Vol. 314/315/316). Integrated Ocean Drilling Program Management International. https://doi.org/10.2204/iodp.proc.314315316.2009

Knittel, K., & Boetius, A. (2009). Anaerobic oxidation of methane: Progress with an unknown process. *Annual Review of Microbiology*, *63*(1), 311–334. https://doi.org/10.1146/annurev.micro.61.080706.093130

Köster, M., Kars, M., Schubotz, F., Tsang, M.-Y., Maisch, M., Kappler, A., et al. (2021a). Evolution of (bio-)geochemical processes and diagenetic alteration of sediments along the tectonic migration of ocean floor in the Shikoku Basin off Japan. *Geochemistry, Geophysics, Geosystems*, *22*. https://doi.org/10.1029/2020GC009585

Köster, M., Kars, M., Schubotz, F., Tsang, M.-Y., Maisch, M., Kappler, A., et al. (2021b). *Rock magnetic end-member unmixing of sediment cores from IODP Hole 370-C0023A*. PANGAEA. https://doi.org/10.1594/PANGAEA.929317

Larrasoaña, J. C., Roberts, A. P., Musgrave, R. J., Gràcia, E., Piñero, E., Vega, M., & Martínez-Ruiz, F. (2007). Diagenetic formation of greigite and pyrrhotite in marine sedimentary systems containing gas hydrates. *Earth and Planetary Science Letters*, *261*(3–4), 350–366. https://doi.org/10.1016/j.epsl.2007.06.032

Lascu, I., Einsle, J. F., Ball, M. R., & Harrison, R. J. (2018). The vortex state in geologic materials: A micromagnetic perspective. *Journal of Geophysical Research: Solid Earth*, *123*, 7285–7304. https://doi.org/10.1029/2018JB015909

Lin, Z., Sun, X., Roberts, A. P., Strauss, H., Lu, Y., Yang, X., et al. (2021). A novel authigenic magnetite source for sedimentary magnetization. *Geology*, *49*(4), 360–365. https://doi.org/10.1130/G48069.1

Lovley, D. R. (1991). Dissimilatory Fe(III) and Mn(IV) Reduction. *Microbiological Reviews*, *55*(2), 259–287. https://doi.org/10.1128/mr.55.2.259-287.1991

Lu, R., & Banerjee, S. K. (1994). Magnetite dissolution in deep sediments and its hydrologic implication: A detailed study of sediments from site 808, leg 131. *Journal of Geophysical Research*, *99*(B5), 9051–9059. https://doi.org/10.1029/93jb03204

Luo, M., Torres, M. E., Hong, W.-L., Pape, T., Fronzek, J., Kutterolf, S., et al. (2020). Impact of iron release by volcanic ash alteration on carbon cycling in sediments of the northern Hikurangi margin. *Earth and Planetary Science Letters*, *541*, 116288. https://doi.org/10.1016/j.epsl.2020.116288

McCabe, C., Jackson, M., & Saffer, B. (1989). Regional patterns of magnetite authigenesis in the Appalachian basin: Implications for the mechanism of Late Paleozoic remagnetization. *Journal of Geophysical Research*, *94*(B8), 10429–10443. https://doi.org/10.1029/jb094ib08p10429

McCabe, C., Sassen, R., & Saffer, B. (1987). Occurrence of secondary magnetite within biodegraded oil. *Geology*, *15*, 7–10. https://doi.org/10.1130/0091-7613(1987)15<7:oosmwb>2.0.co;2

McKay, L., Klokman, V. W., Mendlovitz, H. P., LaRowe, D. E., Hoer, D. R., Albert, D., et al. (2016). Thermal and geochemical influences on microbial biogeography in the hydrothermal sediments of Guaymas Basin, Gulf of California. *Environmental Microbiology Reports*, *8*, 150–161. https://doi.org/10.1111/1758-2229.12365

Moore, G. F., Taira, A., Klaus, A., Becker, K., Becker, L., Boeckel, B., et al. (2001). *Proceedings of the Ocean Drilling Program, initial reports* (Vol. 190). Ocean Drilling Program. https://doi.org/10.2973/odp.proc.ir.190.2001

Muxworthy, A. R., & Dunlop, D. J. (2002). First-order reversal curve (FORC) diagrams for pseudosingle-domain magnetites at high temperature. *Earth and Planetary Science Letters*, *203*, 369–382. https://doi.org/10.1016/s0012-821x(02)00880-4

Muxworthy, A. R., & McClelland, E. (2000). Review of the low-temperature magnetic properties of magnetite from a rock magnetic perspective. *Geophysical Journal International*, *140*(1), 101–114. https://doi.org/10.1046/j.1365-246x.2000.00999.x

Özdemir, Ö., Dunlop, D. J., & Moskowitz, B. M. (2002). Changes in remanence, coercivity and domain state at low temperature in magnetite. *Earth and Planetary Science Letters*, *194*, 343–358. https://doi.org/10.1016/s0012-821x(01)00562-3

Parkes, R. J., Wellsbury, P., Mather, I. D., Cobb, S. J., Cragg, B. A., Hornibrook, E. R. C., & Horsfield, B. (2007). Temperature activation of organic matter and minerals during burial has the potential to sustain the deep biosphere over geological timescales. *Organic Geochemistry*, *38*, 845–852. https://doi.org/10.1016/j.orggeochem.2006.12.011

Peters, K. E. (1986). Guidelines for evaluating petroleum source rocks using programmed pyrolysis. *American Association of Petroleum Geologists Bulletin*, *70*, 318–329. https://doi.org/10.1306/94885688-1704-11d7-8645000102c1865d

Pike, C. R., Roberts, A. P., & Verosub, K. L. (1999). Characterizing interactions in fine magnetic particle systems using first order reversal curves. *Journal of Applied Physics*, *85*(9), 6660–6667. https://doi.org/10.1063/1.370176

Reed, D. W., Fujita, Y., Delwiche, M. E., Blackwelder, D. B., Sheridan, P. P., Uchida, T., & Colwell, F. S. (2002). Microbial communities from methane hydrate–bearing deep-marine sediments in a forearc basin. *Applied and Environmental Microbiology*, *68*(8), 3759–3770. https://doi.org/10.1128/AEM.68.8.3759-3770.2002

Riedinger, N., Brunner, B., Formolo, M. J., Solomon, E., Kasten, S., Strasser, M., & Ferdelman, T. G. (2010). Oxidative sulfur cycling in the deep biosphere of the Nankai Trough, Japan. *Geology*, *38*, 851–854. https://doi.org/10.1130/g31085.1

Riedinger, N., Pfeifer, K., Kasten, S., Garming, J. F. L., Vogt, C., & Hensen, C. (2005). Diagenetic alteration of magnetic signals by anaerobic oxidation of methane related to a change in sedimentation rate. *Geochimica et Cosmochimica Acta*, *69*(16), 4117–4126. https://doi.org/10.1016/j.gca.2005.02.004

Roberts, A. P. (2015). Magnetic mineral diagenesis. *Earth-Science Reviews*, *151*, 1–47. https://doi.org/10.1016/j.earscirev.2015.09.010

Roberts, A. P., Almeida, T. P., Church, N. S., Harrison, R. J., Heslop, D., Li, Y., et al. (2017). Resolving the origin of pseudo-single domain magnetic behavior. *Journal of Geophysical Research: Solid Earth*, *122*, 9534–9558. https://doi.org/10.1002/2017JB014860

Roberts, A. P., Chang, L., Rowan, C. J., Horng, C.-S., & Florindo, F. (2011). Magnetic properties of sedimentary greigite (Fe_3S_4): An update. *Reviews of Geophysics*, *49*, RG1002. https://doi.org/10.1029/2010rg000336.1

Roberts, A. P., Liu, Q., Rowan, C. J., Chang, L., Carvallo, C., Torrent, J., & Horng, C. S. (2006). Characterization of hematite (α-Fe_2O_3), goethite (α-FeOOH), greigite (Fe_3S_4), and pyrrhotite (Fe_7S_8) using first-order reversal curve diagrams. *Journal of Geophysical Research*, *111*, B12S35. https://doi.org/10.1029/2006JB004715

Roberts, A. P., Pike, C. R., & Verosub, K. L. (2000). First-order reversal curve diagrams: A new tool for characterizing the magnetic properties of natural samples. *Journal of Geophysical Research*, *105*(B12), 28461–28475. https://doi.org/10.1029/2000JB900326

Roberts, A. P., Tauxe, L., Heslop, D., Zhao, X., & Jiang, Z. (2018). A critical appraisal of the "Day" diagram. *Journal of Geophysical Research: Solid Earth*, *123*, 2618–2644. https://doi.org/10.1002/2017JB015247

Roberts, A. P., & Weaver, R. (2005). Multiple mechanisms of remagnetization involving sedimentary greigite (Fe_3S_4). *Earth and Planetary Science Letters*, *231*(3–4), 263–277. https://doi.org/10.1016/j.epsl.2004.11.024

Rochette, P., Fillion, G., Mattéi, J.-L., & Dekkers, M. J. (1990). Magnetic transition at 30–34 Kelvin in pyrrhotite: Insight into a widespread occurrence of this mineral in rocks. *Earth and Planetary Science Letters*, *98*(3–4), 319–328. https://doi.org/10.1016/0012-821X(90)90034-U

Rowan, C. J., & Roberts, A. P. (2005). Tectonic and geochronological implications of variably timed magnetizations carried by authigenic greigite in marine sediments from New Zealand. *Geology*, *33*(7), 553–556. https://doi.org/10.1130/G21382.1

Rowan, C. J., Roberts, A. P., & Broadbent, T. (2009). Reductive diagenesis, magnetite dissolution, greigite growth and paleomagnetic smoothing in marine sediments: A new view. *Earth and Planetary Science Letters*, *277*(1–2), 223–235. https://doi.org/10.1016/j.epsl.2008.10.016

Seno, T., Stein, S., & Gripp, A. E. (1993). A model for the motion of the Philippine Sea plate consistent with NUVEL-1 and geological data. *Journal of Geophysical Research*, *98*(B10), 17941–17948. https://doi.org/10.1029/93JB00782

Shipboard Scientific Party (1991). Site 808. In A. Taira, I. Hill, J. V. Firth, U. Berner, W. Brückmann, T. Byrne, et al. (Eds.), *Proceedings of the Ocean Drilling Program, initial reports* (Vol. 131, pp. 71–269). Ocean Drilling Program. https://doi.org/10.2973/odp.proc.ir.131.106.1991

Shipboard Scientific Party (2001). Site 1174. In G. F. Moore, A. Taira, A. Klaus, K. Becker, L. Becker, B. Boeckel, et al. (Eds.), *Proceedings of the Ocean Drilling Program, initial reports* (Vol. 190, pp. 1–149). Ocean Drilling Program. https://doi.org/10.2973/odp.proc.ir.190.105.2001

Stein, R. (2021). *Rock-Eval data of IODP Hole 370-C0023A*. PANGAEA. Retrieved from https://doi.pangaea.de/10.1594/PANGAEA.936510

Stein, R., Rullkötter, J., & Welte, D. H. (1986). Accumulation of organic-carbon-rich sediments in the Late Jurassic and Cretaceous Atlantic Ocean—A synthesis. *Chemical Geology*, *56*, 1–32. https://doi.org/10.1016/0009-2541(86)90107-5

Taira, A., Hill, I., Firth, J. V., Berner, U., Brückmann, W., Byrne, T., et al. (1991). *Proceedings of the Ocean Drilling Program, initial reports* (Vol. 131). Ocean Drilling Program. https://doi.org/10.2973/odp.proc.ir.131.1991

Tissot, B. P., Pelet, R., & Ungerer, P. (1987). Thermal history of sedimentary basins, maturation indexes, and kinetics of oil and gas generation. *AAPG Bulletin*, *71*, 1445–1466. https://doi.org/10.1306/703c80e7-1707-11d7-8645000102c1865d

Tissot, B. P., & Welte, D. H. (1984). *Petroleum formation and occurrence* (p. 699). Springer-Verlag.

Treude, T., Niggemann, J., Kallmeyer, J., Wintersteller, P., Schubert, C. J., Boetius, A., & Jørgensen, B. B. (2005). Anaerobic oxidation of methane in the sulfate-methane transition along the Chilean continental margin. *Geochimica et Cosmochimica Acta*, *69*(11), 2767–2779. https://doi.org/10.1016/j.gca.2005.01.002

Tsang, M.-Y., Bowden, S. A., Wang, Z., Mohammed, A., Tonai, S., Muirhead, D., et al. (2020). Hot fluids, burial metamorphism and thermal histories in the underthrust sediments at IODP 370 Site C0023, Nankai Accretionary Complex. *Marine and Petroleum Geology*, *112*, 104080. https://doi.org/10.1016/j.marpetgeo.2019.104080

van Velzen, A. J., & Zijderveld, J. D. A. (1992). A method to study alterations of magnetic minerals during thermal demagnetization applied to a fine-grained marine marl (Trubi formation, Sicily). *Geophysical Journal International*, *110*, 79–90. https://doi.org/10.1111/j.1365-246x.1992.tb00715.x

Wehland, F., Stancu, A., Rochette, P., Dekkers, M. J., & Appel, E. (2005). Experimental evaluation of magnetic interaction in pyrrhotite bearing samples. *Physics of the Earth and Planetary Interiors*, *153*, 181–190. https://doi.org/10.1016/j.pepi.2005.05.006

Zhao, X., Heslop, D., & Roberts, A. P. (2015). A protocol for variable resolution first-order reversal curve measurements. *Geochemistry, Geophysics, Geosystems*, *16*, 1364–1377. https://doi.org/10.1002/2014GC005680

Zhao, X., Roberts, A. P., Heslop, D., Paterson, G. A., Li, Y., & Li, J. (2017). Magnetic domain state diagnosis using hysteresis reversal curves. *Journal of Geophysical Research: Solid Earth*, *122*, 4767–4789. https://doi.org/10.1002/2016JB013683

Reference From the Supporting Information

Moskowitz, B., Frankel, R. B., & Bazylinski, D. A. (1993). Rock magnetic criteria for the detection of biogenic magnetite. *Earth and Planetary Science Letters*, *120*, 283–300. https://doi.org/10.1016/0012-821x(93)90245-5